

Probabilistic Hierarchical Interpolation and Interpretable Neural Network Configurations for Flood Prediction

Mostafa Saberian¹, Vidya Samadi^{2,3*}, Ioana Popescu³ Popescu⁴

1. The Glenn Department of Civil Engineering, Clemson University, Clemson, SC

2. Department of Agricultural Sciences, Clemson University, Clemson, SC.

3. Artificial Intelligence Research Institute for Science and Engineering (AIRISE), Clemson University, Clemson, SC, USA

Formatted: Font: (Default) +Headings CS (Times New Roman), 11 pt

[3.4.](#) Department of Hydroinformatics and Socio-Technical Innovation, IHE Delft Institute for Water Education, Delft, the Netherlands

*Corresponding author: samadi@clemson.edu

Abstract

13 The past few years have witnessed the rise of neural networks (NNs) applications for hydrological time
14 series modeling. By virtue of their capabilities, NN models can achieve unprecedented levels of
15 performance when learning how to solve increasingly complex rainfall-runoff processes via data, making
16 them pivotal for the development of computational hydrologic tasks such as flood predictions. The NN
17 models should, to be considered practical, provide a probabilistic understanding of the model mechanisms
18 and predictions and hints on what could perturb the model. In this paper, we developed two NN models,
19 i.e., Neural Hierarchical Interpolation for Time Series Forecasting (N-HiTS) and Network-Based
20 Expansion Analysis for Interpretable Time Series Forecasting (N-BEATS) with a probabilistic multi-
21 quantile objective and benchmarked them with long short-term memory (LSTM) for flood prediction across
22 two headwater streams in Georgia and North Carolina, USA. To generate a probabilistic prediction, a Multi-
23 Quantile Loss was used to assess the 95th percentile prediction uncertainty (95PPU) of multiple flooding
24 events. Extensive experiments demonstrated the advantages of hierarchical interpolation and interpretable
25 architecture, where both N-HiTS and N-BEATS provided an average accuracy improvement of ~5% over
26 the LSTM benchmarking model. On a variety of flooding events, both N-HiTS and N-BEATS demonstrated
27 significant performance improvements over the LSTM benchmark and showcased their probabilistic
28 predictions by specifying a likelihood objective.

Keywords: Probabilistic Flood Prediction; Neural Networks; N-HiTS; N-BEATS; LSTM; Headwater Stream.

31 **Key Points**

32

- N-HiTS and N-BEATS predictions reflect interpretability and hierarchical representations of data
33 to reduce neural network complexities.
- Both N-HiTS and N-BEATS models outperformed the LSTM in mathematically defining
35 uncertainty bands.
- Predicting the magnitude of the recession curve of flood hydrographs was particularly challenging
37 for all models.

38 **Plain Language Summary**

39 Recent progress in NN accelerated improvements in the performance of catchment modeling. Yet flood
40 modeling remains a very difficult task. Focusing on two headwater streams, we developed N-HiTS and N-
41 BEATS models and benchmarked them with LSTM to predict flooding. N-HiTS and N-BEATS
42 outperformed LSTM for flood predictions. We demonstrated how the proposed models can be augmented
43 with an uncertainty approach to predict flooding that is interpretable without considerable loss in accuracy.

44

45 **1. Introduction**

46 The past few years have witnessed a rapid surge in the neural networks (NN) applications in hydrology. As
47 these opaque, data-driven models are increasingly employed for critical hydrological predictions, the
48 hydrology community has placed growing emphasis on developing trustworthy and interpretable NN
49 models. However, maintaining coherence while producing accurate predictions can be a challenging
50 problem (Olivares et al., 2024). There is a general agreement on the importance of providing probabilistic
51 NN prediction (Sadeghi Tabas and Samadi, 2022), especially in the case of flood prediction (Martinaitis et
52 al., 2023).

53 Flood occurrences have witnessed an alarming surge in frequency and severity globally. Jonkman (2005)
54 studied a natural disaster database (EM-DAT, 2023) and reported that over 27 years, more than 175000
55 people died, and close to 2.2 billion were affected directly by floods worldwide. These numbers are likely
56 an underestimation due to unreported events (Nevo et al., 2022). In addition, the United Nations Office for
57 Disaster Risk Reduction reported that flooding has been the most frequent, widespread weather-related
58 natural disaster since 1995, claiming over 600,000 lives, affecting around 4 billion people globally, and
59 causing annual economic damage of more than 100 billion USD (UNISDR, 2015). This escalating trend
60 has necessitated the need for better flood prediction and management strategies. Scholars have successfully
61 implemented different flood models such as deterministic (e.g., Roelvink et al., 2009, Thompson and
62 Frazier, 2014; Barnard et al., 2014; Erikson et al., 2018) and physically based flood models (e.g., Basso et
63 al., 2016; Chen et al., 2016; Pourreza-Bilondi et al., 2017; Saksena et al., 2019; Refsgaard et al., 2021) in

64 various environmental systems over the past several decades. These studies have heightened the need for
65 precise flood prediction (Samadi et al., 2025), they have also unveiled limitations inherent in existing
66 deterministic and physics-based models.

67 While evidence suggests that both deterministic and physics-based approaches are meaningful and useful
68 (Sukovich et al., 2014; Zafarmomen et al., 2024), their forecasts rest heavily on imprecise and subjective
69 expert opinion; there is a challenge for setting robust evidence-based thresholds to issue flood warnings and
70 alerts (Palmer, 2012). Moreover, many of these traditional flood models, particularly physically explicit
71 models, rely too strongly on a particular choice of numerical approximation and describe multiple process
72 parameterizations only within a fixed spatial architecture (e.g., Clark et al., 2015). Recent NN models have
73 shown promising results across a large variety of flood modeling applications (e.g., Nevo et al., 2022; Pally
74 and Samadi, 2022; Dasgupta et al., 2023; Zhang et al., 2023; Zafarmomen and Samadi, 2025; Saberian et
75 al., 2025) and encourage the use of such methodologies as core drivers for neural flood prediction
76 (Windheuser et al., 2023).

77 Earlier adaptations of these intelligent techniques showed promising for flood prediction (e.g., Hsu et al.,
78 1995; Tiwari and Chatterjee, 2010). However, recent efforts have taken NN application to the next level,
79 providing uncertainty assessment (Sadeghi Tabas and Samadi, 2022) and improvements over various
80 spatio-temporal scales, regions, and processes (e.g., Kratzert et al., 2018; Park and Lee, 2023; Zhang et al.,
81 2023). Nevo et al., (2022) were the first scholars who employed long short-term memory (LSTM) for flood
82 stage prediction and inundation mapping, achieving notable success during the 2021 monsoon season. Soon
83 after, Russo et al. (2023) evaluated various NN models for predicting depth flood in urban systems,
84 highlighting the potential of data-driven models for urban flood prediction. Similarly, Defontaine et al.
85 (2023) emphasized the role of NN algorithms in enhancing the reliability of flood predictions, particularly
86 in the context of limited data availability. Windheuser et al., (2023) studied flood gauge height forecasting
87 using images and time series data for two gauging stations in Georgia, USA. They used multiple NN models
88 such as Convolutional Neural Network (ConvNet/CNN) and LSTM to forecast floods in near real-time (up
89 to 72 hours).

90 In a sequence, Wee et al., (2023) used Impact-Based Forecasting (IBF) to propose a Flood Impact-Based
91 Forecasting system (FIBF) using flexible fuzzy inference techniques, aiding decision-makers in a timely
92 response. Zou et al. (2023) proposed a Residual LSTM (ResLSTM) model to enhance and address flood
93 prediction gradient issues. They integrated Deep Autoregressive Recurrent (DeepAR) with four recurrent
94 neural networks (RNNs), including ResLSTM, LSTM, Gated Recurrent Unit (GRU), and Time
95 Feedforward Connections Single Gate Recurrent Unit (TFC-SGRU). They showed that ResLSTM achieved
96 superior accuracy. While these studies reported the superiority of NN models for flood modeling, they

97 highlighted a number of challenges, notably (i) the limited capability of proposed NN models to capture
98 the spatial variability and magnitudes of extreme data over time, (ii) the lack of a sophisticated mechanism
99 to capture different flood magnitudes and synthesize the prediction, and (iii) inability of the NN models to
100 process data in parallel and capture the relationships between all elements in a sequential manner.

101 Recent advances in neural time series forecasting showed promising results that can be used to address the
102 above challenges for flood prediction. Recent techniques include the adoption of the attention mechanism
103 and Transformer-inspired approaches (Fan et al. 2019; Alaa and van der Schaar 2019; Lim et al. 2021)
104 along with attention-free architectures composed of deep stacks of fully connected layers (Oreshkin et al.
105 2020).

106 All these approaches are relatively easy to scale up in terms of flood magnitudes (small to major flood
107 predictions), compared to LSTM and have proven to be capable of capturing spatiotemporal dependencies
108 (Challu et al., 2022). In addition, these architectures can capture input-output relationships implicitly while
109 they tend to be more computationally efficient. Many state-of-the-art NN approaches for flood forecasting
110 have been established based on LSTM. There are cell states in the LSTM networks that can be interpreted
111 as storage capacity often used in flood generation schemes. In LSTM, the updating of internal cell states
112 (or storages) is regulated through several gates: the first gate regulates the storage depletion, the second one
113 regulates storage fluctuations, and the third gate regulates the storages outflow (Tabas and Samadi, 2022).
114 The elaborate gated design of the LSTM partly solves the long-term dependency problem in flood time
115 series prediction (Fang et al., 2020), although, the structure of LSTMs is designed in a sequential manner
116 that cannot directly connect two nonadjacent portions (positions) of a time series.

117 In this paper, we developed attention-free architecture, i.e. Neural Hierarchical Interpolation for Time
118 Series Forecasting (N-HiTS; Challu et al., 2022) and Network-Based Expansion Analysis for Interpretable
119 Time Series Forecasting (N-BEATS; Oreshkin et al., 2020) and benchmarked these models with LSTM for
120 flood prediction. We developed fully connected N-BEATS and N-HiTS architectures using multi-rate data
121 sampling, synthesizing the flood prediction outputs via multi-scale interpolation.

122 We implemented all algorithms for flood prediction on two headwater streams i.e., the Lower Dog River,
123 Georgia, and the Upper Dutchmans Creek, North Carolina, USA to ensure that the results are reliable and
124 comparable. The results of N-BEATS and N-HiTS techniques were compared with the benchmarking
125 LSTM to understand how these techniques can improve the representations of rainfall and runoff
126 dispensing over a recurrence process. Notably, this study represents a pioneering effort, as to the best of
127 our knowledge, this is the first instance in which the application of N-BEATS and N-HiTS algorithms in
128 the field of flood prediction has been explored. The scope of this research will focus on:

129 (i) **Flood prediction in a hierarchical fashion with interpretable outputs:** We built N-BEATS and
130 N-HiTS for flood prediction with a very deep stack of fully connected layers to implicitly capture input-
131 output relationships with hierarchical interpolation capabilities. The predictions also involve programming
132 the algorithms with decreasing complexity and aligning their time scale with the final output through multi-
133 scale hierarchical interpolation and interpretable architecture. Predictions were aggregated in a hierarchical
134 fashion that enabled the building of a very deep neural network with interpretable configurations.

135 (ii) **Uncertainty quantification of the models by employing probabilistic approaches:** a Multi-
136 Quantile Loss (MQL) was used to assess the 95th percentile prediction uncertainty (95PPU) of multiple
137 flooding events. MQL was integrated as the loss function to account for probabilistic prediction. MQL
138 trains the model to produce probabilistic forecasts by predicting multiple quantiles of the distribution of
139 future values.

140 (iii) **Exploring headwater stream response to flooding:** Understanding the dynamic response of
141 headwater streams to flooding is essential for managing downstream flood risks. Headwater streams
142 constitute the uppermost sections of stream networks, usually comprising 60% to 80% of a catchment area.
143 Given this substantial coverage and the tendency for precipitation to increase with elevation, headwater
144 streams are responsible for generating and controlling the majority of runoff in downstream portions
145 (MacDonald and Coe, 2007).

146 The remainder of this paper is structured as follows. Section 2 presents the case study and data, NN models,
147 performance metrics, and sensitivity and uncertainty approaches. Section 3 focuses on the results of flood
148 predictions including sensitivity and uncertainty assessment and computation efficiency. Finally, Section 4
149 concludes the paper.

150

151 2. Methodology

152 2.1. Case Study and Data

153 This research used two headwater gauging stations located at the Lower Dog River watershed, Georgia
154 (GA; USGS02337410, Dog River gauging station), and the Upper Dutchmans Creek watershed, North
155 Carolina (NC; USGS0214269560, Killian Creek gauging station). As depicted in Figures 1, the Lower Dog
156 River and the Upper Dutchmans Creek watersheds are in the west and north parts of two metropolitan cities,
157 Atlanta and Charlotte. The Lower Dog River stream gauge is established southeast of Villa Rica in Carroll
158 County, where the USGS has regularly monitored discharge data since 2007 in 15-minute increments. The
159 Lower Dog River is a stream with a length of 15.7 miles (25.3 km; obtained from the U.S. Geological
160 Survey [USGS] National Hydrography Dataset high-resolution flowline data), an average elevation of

161 851.94 meters, and the watershed area above this gauging station is 66.5 square miles (172 km²; obtained
162 from the Georgia Department of Natural Resources). This watershed is covered by 15.2% residential area,
163 14.6% agricultural land, and ~70% forest (Munn et al., 2020).

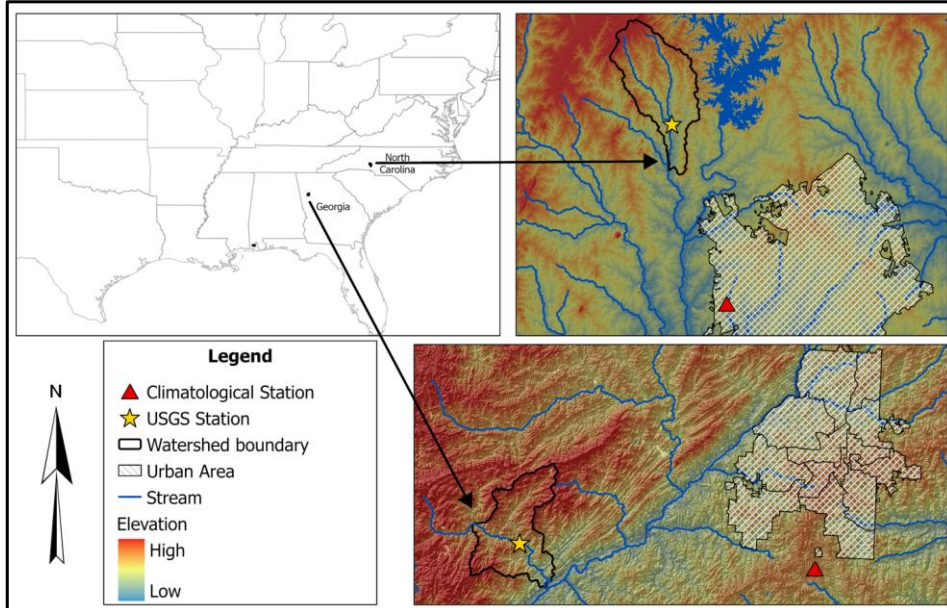
164 Killian Creek gauging station at the Upper Dutchmans Creek watershed is established in Montgomery
165 County, NC, where the USGS has regularly monitored discharge data since 1995 in 15-minute increments.
166 The Upper Dutchmans Creek is a stream with a length of 4.9 miles (7.9 km), an average elevation of 642.2
167 meters (see Table 1), and the watershed area above this gauging station is 4 square miles (10.3 km²) with
168 less than 3% residential area and about 93% forested land use (the United States Environmental Protection
169 Agency).

170 The Lower Dog River has experienced significant flooding in the last decades. For example, in September
171 2009, the creek, along with most of northern GA, experienced heavy rainfall (5 inches, equal to 94 mm).
172 The Lower Dog River, overwhelmed by large amounts of overland flow from saturated ground in the
173 watershed, experienced massive flooding in September 2009 (Gotvald, 2010). The river crested at 33.8 feet
174 (10.3 m) with a peak discharge of 59,900 cfs (1,700 m³/s), nearly six times the 100-year flood level
175 (McCallum and Gotvald, 2010). In addition, Dutchmans Creek experienced significant flooding in February
176 2020. According to local news (WCCB Charlotte, 2020), the flood in Gaston County caused significant
177 infrastructure damage and community disruption. Key impacts included the threatened collapse of the
178 Dutchman's Creek bridge in Mt. Holly and the closure of Highway 7 in McAdenville, GA.

179
180 Table 1. The Lower Dog River and Upper Dutchmans Creek's physical characteristics.

Watershed	USGS Station ID Number	Average Elevation (m)	Stream Length (km)	Watershed area (km ²)
Lower Dog River watershed, GA	USGS02337410	851.9	25.3	172
Upper Dutchmans Creek watershed, NC	USGS0214269560	642.2	7.9	10.3

181



182

183 Figure 1. The Lower Dog River and The Upper Dutchmans Creek watersheds are in GA and NC. The
 184 proximity of the watersheds to Atlanta and Charlotte (urban area) are also displayed on the map.

185 To provide the meteorological forcing data, i.e., precipitation, temperature, and humidity, were extracted
 186 from the National Oceanic and Atmospheric Administration's (NOAA) Local Climatological Data
 187 (LCD). We used the NOAA precipitation, temperature, and humidity data of Atlanta Hartsfield Jackson
 188 International Airport and Charlotte Douglas Airport stations as an input for neural network algorithms. The
 189 data has been monitored since January 1, 1948, and July 22, 1941, with an hourly interval which was used
 190 as an input variable for constructing neural networks.

191 To fill in the missing values in the data, we used the spline interpolation method. We applied this method
 192 to fill the gaps in time series data, although the missing values were insignificant (less than 1%). In addition,
 193 we employed the Minimum Inter-Event Time (MIT) approach to precisely identify and separate individual
 194 storm events. The MIT-based event delineation is pivotal for accurately defining storm events. This method
 195 allowed us to isolate discrete rainfall episodes, aiding a comprehensive analysis of storm events. Moreover,
 196 it provided a basis for event-specific examination of flood responses, such as initial condition and cessation
 197 (loss), runoff generation, and runoff dynamics.

198 The hourly rainfall dataset consists of distinct rainfall occurrences, some consecutive and others clustered
199 with brief intervals of zero rainfall. As these zero intervals extend, we aim to categorize them into distinct
200 events. It's worth noting that even within a single storm event, we often encounter short periods of no
201 rainfall, known as intra-storm zero values. In the MIT method, we defined a storm event as a discrete rainfall
202 episode surrounded by dry periods both preceding and following it, determined by an MIT (Asquith et al.,
203 2005; Safaei-Moghadam et al., 2023).

204 There are many ways to determine MIT value. One practical approximation is using serial autocorrelation
205 between rainfall occurrences. MIT approach uses autocorrelation that measures the statistical dependency
206 of rainfall data at one point in time with data at earlier, or lagged times within the time series. The lag time
207 represents the gap between data points being correlated. When the lag time is zero, the autocorrelation
208 coefficient is unity, indicating a one-to-one correlation. As the lag time increases, the statistical correlation
209 diminishes, converging to a minimum value. This signifies the fact that rainfall events become
210 progressively less statistically dependent or, in other words, temporally unrelated. To pinpoint the optimal
211 MIT, we analyzed the autocorrelation coefficients for various lag times, observing the point at which the
212 coefficient approaches zero. This lag time signifies the minimum interval of no rainfall, effectively
213 delineating distinct rainfall events.

214

215 **2.2. NN Algorithms**

216 In this study, three distinct neural network (NN) architectures were developed to perform multi-horizon
217 flood forecasting. Each NN was coupled with a MQL objective to generate probabilistic predictions and
218 quantify predictive uncertainty. Throughout the manuscript, the term parameters are used exclusively to
219 refer to the network's weights and biases for clarity and consistency.

220

221 **2.2.1. LSTM**

222 LSTM is an RNN architecture widely used as a benchmark model for flood neural time series
223 modeling. LSTM networks are capable of selectively learning order dependence in sequence prediction
224 problems (Sadeghi Tabas and Samadi, 2022). These networks are powerful because they can capture the
225 temporal features, especially the long-term dependencies (Hochreiter et al., 2001) and are independent of
226 the length of the data sequences input, meaning that each sample is independent from another one.

227 The memory cell state within LSTM plays a crucial role in capturing extended patterns in data, making it
228 well-suited for dynamic time series modeling such as flood prediction. An LSTM cell uses the following
229 functions to compute flood prediction.

$$i_t = \sigma(A_i x_t + B_i h_{t-1} + c_i) \quad (\text{Equation 1})$$

$$f_t = \sigma(A_f x_t + B_f h_{t-1} + c_f) \quad (\text{Equation 2})$$

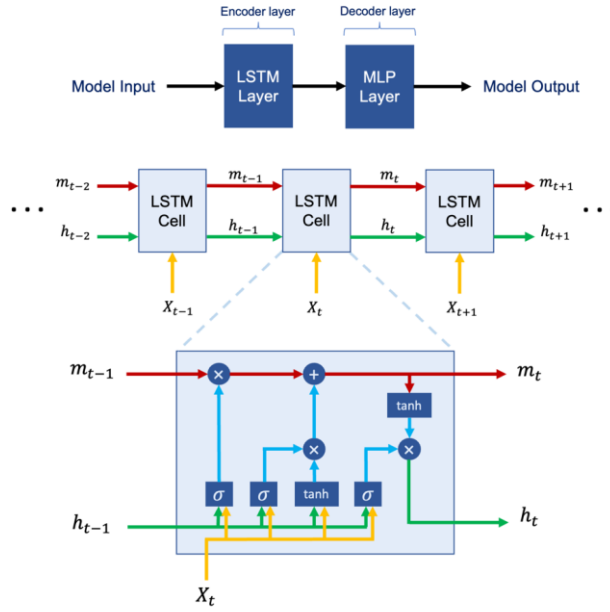
$$o_t = \sigma(A_o x_t + B_o h_{t-1} + c_o) \quad (\text{Equation 3})$$

$$m_t = f_t \odot m_{t-1} + i_t \odot \tanh(A_g x_t + B_g h_{t-1} + c_g) \quad (\text{Equation 4})$$

$$h_t = o_t \odot \tanh(m_t) \quad (\text{Equation 5})$$

230 Where x_t and h_t represent the input and the hidden state at time step t , respectively. \odot denotes element-
231 wise multiplication, \tanh stands for the hyperbolic tangent activation function, and σ represents the
232 sigmoid activation function. A , B , and c are trainable weights and biases that undergo optimization during
233 the training process. m_t and h_t are cell states at time step t that are employed in the input processing for
234 the next time step. m_t represents the memory state responsible for preserving long-term information, while
235 h_t represents the memory state preserving short-term information. The LSTM cell consists of a forget gate
236 f_t , an input gate i_t and an output gate o_t and has a cell state m_t . At every time step t , the cell gets the data
237 point x_t with the output of the previous cell h_{t-1} (Windheuser et al., 2023). The forget gate then defines if
238 the information is removed from the cell state, while the input gate evaluates if the information should be
239 added to the cell state and the output gate specifies which information from the cell state can be used for
240 the next cells.

241 We used two LSTM layers with 128 cells in the first two hidden layers as encoder layers, which were then
242 connected to two multilayer perceptron (MLP) layers with 128 neurons as decoder layers. The LSTM
243 simulation was performed with these input layers along with the *Adam* optimizer (Kingma and Ba,
244 2014), \tanh activation function, and a single lagged dependent-variable value to train with a learning rate
245 of 0.001. The architecture of the proposed LSTM model is illustrated in Figure 2.



246

247 Figure 2. The structure of LSTM programmed in this research. We used *tanh* and *sigmoid* as activation
 248 functions along with 2 layers of LSTM, 2 layers of MLP, and 128 cells in each layer.

249

250 2.2.2. N-BEATS

251 N-BEATS is a deep learning architecture based on backward and forward residual links and the very deep
 252 stack of fully connected layers specifically designed for sequential data forecasting tasks (Oreshkin et al.,
 253 2020). This architecture has several desirable properties including interpretability. The N-BEATS
 254 architecture distinguishes itself from existing architecture in several ways. First, the algorithm approaches
 255 forecasting as a non-linear multivariate regression problem instead of a sequence-to-sequence
 256 challenge. Indeed, the core component of this architecture (as depicted in Figure 3) is a fully connected
 257 non-linear regressor, which takes the historical data from a time series as input and generates multiple data
 258 points for the forecasting horizon. Second, most existing time series architectures are quite limited in depth,
 259 typically consisting of one to five LSTM layers. N-BEATS employs the residual principle to stack a
 260 substantial number of layers together, as illustrated in Figure 3. In this configuration, the basic block not
 261 only predicts the next output but also assesses its contribution to decomposing the input, a concept that is
 262 referred to as "backcast" (see Oreshkin et al. 2020).

263 The basic building block in the architecture features a fork-like structure, as illustrated in Figure 3 (bottom).
 264 The l -th block (for the sake of brevity, the block index l is omitted from Figure 3) takes its respective input,
 265 x_l , and produces two output vectors: \hat{x}_l and \hat{y}_l . In the initial block of the model, x_l corresponds to the
 266 overall model input, which is a historical lookback window of a specific length, culminating with the most
 267 recent observed data point. For the subsequent blocks, x_l is derived from the residual outputs of the
 268 preceding blocks. Each block generates two distinct outputs: 1. \hat{y}_l : This represents the forward forecast of
 269 the block, spanning a duration of H time units. 2. \hat{x}_l : This signifies the block's optimal estimation of x_l ,
 270 which is referred to "backcast." This estimation is made within the constraints of the functional space
 271 available to the block for approximating signals (Oreshkin et al., 2020).

272 Internally, the fundamental building block is composed of two elements. The initial element involves a
 273 fully connected network, which generates forward expansion coefficient predictors, θ_l^f , and a backward
 274 expansion coefficient predictor, θ_l^b . The second element encompasses both backward basis layers, g_l^b , and
 275 forward basis layers, g_l^f . These layers take the corresponding forward θ_l^f and backward θ_l^b expansion
 276 coefficients as input, conduct internal transformations using a set of basis functions, and ultimately yield
 277 the backcast, \hat{x}_l , and the forecast outputs, \hat{y}_l , as previously described by Oreshkin et al. (2020). The
 278 following equations describe the first element:

$$h_{l,1} = FC_{l,1}(x_l), \quad h_{l,2} = FC_{l,2}(h_{l,1}), \quad h_{l,3} = FC_{l,3}(h_{l,2}), \quad h_{l,4} = FC_{l,4}(h_{l,3}). \quad (\text{Equation 6})$$

$$\theta_l^b = \text{LINEAR}_l^b(h_{l,4}), \quad \theta_l^f = \text{LINEAR}_l^f(h_{l,4}) \quad (\text{Equation 7})$$

279 The LINEAR layer, in essence, functions as a straightforward linear projection, meaning $\theta_l^f = W_l^f h_{l,4}$. As
 280 for the fully connected (FC) layer, it takes on the role of a conventional FC layer, incorporating RELU non-
 281 linearity as an activation function.

282 The second element performs the mapping of expansion coefficients θ_l^f and θ_l^b to produce outputs using
 283 basis layers, resulting in $\hat{y}_l = g_l^f(\theta_l^f)$ and $\hat{x}_l = g_l^b(\theta_l^b)$. This process is defined by the following equation:

$$\hat{y}_l = \sum_{i=1}^{\dim(\theta_l^f)} \theta_{l,i}^f v_i^f, \quad \hat{x}_l = \sum_{i=1}^{\dim(\theta_l^b)} \theta_{l,i}^b v_i^b \quad (\text{Equation 8})$$

284 Within this context, v_i^f and v_i^b represent the basis vectors for forecasting and backcasting, respectively,
 285 while $\theta_{l,i}^f$ corresponds to the i -th element of θ_l^f .

286 The N-BEATS uses a novel hierarchical doubly residual architecture which is illustrated in Figure 3 (top
 287 and middle). This framework incorporates two residual branches, one traversing the backcast predictions

288 of each layer, while the other traverses the forecast branch of each layer. The following equation describes
 289 this process:

$$x_l = x_{l-1} - \hat{x}_{l-1} \quad , \quad \hat{y} = \sum_l \hat{y}_l \quad (\text{Equation 9})$$

290 As mentioned earlier, in the specific scenario of the initial block, its input corresponds to the model-level
 291 input x . In contrast, for all subsequent blocks, the backcast residual branch x_l can be conceptualized as
 292 conducting a sequential analysis of the input signal. The preceding block eliminates the portion of the signal
 293 \hat{x}_{l-1} that it can effectively approximate, thereby simplifying the prediction task for downstream blocks.
 294 Significantly, each block produces a partial forecast \hat{y}_l , which is initially aggregated at the stack level and
 295 subsequently at the overall network level, establishing a hierarchical decomposition. The ultimate forecast
 296 \hat{y} is the summation of all partial forecasts (Oreshkin et al., 2020).

297 The N-BEATS model has two primary configurations: generic and interpretable. These configurations
 298 determine how the model structures its blocks and how it processes time series data. In the generic
 299 configuration, the model uses a stack of generic blocks that are designed to be flexible and adaptable to
 300 various patterns in the time series data. Each generic block consists of fully connected layers with ReLU
 301 activation functions. The key characteristic of generic configuration is its flexibility. Since the blocks are
 302 not specialized for any specific pattern (like trend or seasonality), they can learn a wide range of patterns
 303 directly from the data (Oreshkin et al., 2020). In the interpretable configuration, the model architecture
 304 integrates distinct trend and seasonality components. This involves structuring the basis layers at the stack
 305 level specifically to model these elements, allowing the stack outputs to be more easily understood.

306 **Trend Model:** In this stack $g_{s,l}^b$ and $g_{s,l}^f$ are polynomials of a small degree p , functions that vary slowly
 307 across the forecast window, to replicate monotonic or slowly varying nature of trends:

$$\hat{y}_{s,l} = \sum_{i=0}^p \theta_{s,l,i}^f t^i \quad (\text{Equation 10})$$

308 The time vector $t = [0, 1, 2, \dots, H-2, H-1]^T/H$ is specified on a discrete grid ranging from 0 to
 309 $(H-1)/H$, projecting H steps into the future. Consequently, the trend forecast represented in matrix form is:

$$\hat{y}_{s,l}^{tr} = T \theta_{s,l}^f \quad (\text{Equation 11})$$

310 Where the polynomial coefficients, $\theta_{s,l}^f$, predicted by an FC network at layer l of stack s , are described by
 311 Equations (6) and (7). The matrix T , consisting of powers of t , is represented as $[1, t, \dots, t^p]$. When p is
 312 small, such as 2 or 3, it compels $\hat{y}_{s,l}^{tr}$ to emulate a trend (Oreshkin et al., 2020).

313 Seasonality model: In this stack $g_{s,l}^b$ and $g_{s,l}^f$ are periodic functions, to capture the cyclical and recurring
 314 characteristics of seasonality, such that $y_t = y_{t-\Delta}$, where Δ is the seasonality period. The Fourier series
 315 serves as a natural foundation for modeling periodic functions:

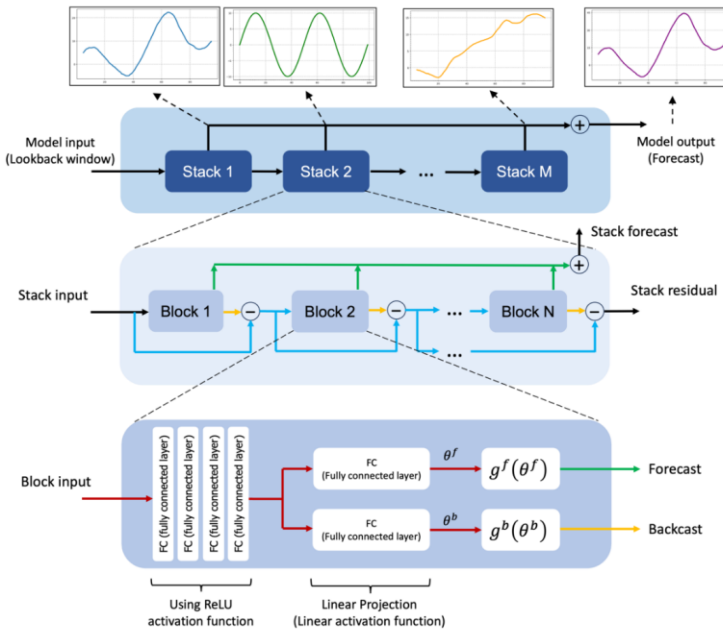
$$\hat{y}_{s,l} = \sum_{i=0}^{\frac{H}{2}-1} \theta_{s,l,i}^f \cos(2\pi i t) + \theta_{s,l,i+\lceil H/2 \rceil}^f \sin(2\pi i t) \quad (\text{Equation 12})$$

316 Consequently, the seasonality forecast is represented in the following matrix form:

$$\hat{y}_{s,l}^{seas} = S \theta_{s,l}^f \quad (\text{Equation 13})$$

$$S = [1, \cos(2\pi t), \dots, \cos\left(2\pi \left[\frac{H}{2} - 1\right] t\right), \sin(2\pi t), \dots, \sin\left(2\pi \left[\frac{H}{2} - 1\right] t\right)] \quad (\text{Equation 14})$$

317 Where the Fourier coefficients $\theta_{s,l}^f$, that predicted by an FC network at layer l of stack s , are described by
 318 Equations (6) and (7). The matrix S represents sinusoidal waveforms. As a result, the forecast $\hat{y}_{s,l}^{seas}$
 319 becomes a periodic function that imitates typical seasonal patterns (Oreshkin et al., 2020).



320

321 Figure 3. The N-BEATS modeling structure, used in this research.

322 **2.2.3. N-HiTS**

323 N-HiTS builds upon the N-BEATS architecture but with improved accuracy and computational efficiency
 324 for long-horizon forecasting. N-HiTS utilizes multi-rate sampling and multi-scale synthesis of forecasts,
 325 leading to a hierarchical forecast structure that lowers computational demands and improves prediction
 326 accuracy (Challu et al., 2022).

327 Like N-BEATS, N-HiTS employs local nonlinear mappings onto foundational functions within numerous
 328 blocks. Each block includes an MLP that generates backcast and forecast output coefficients. The backcast
 329 output refines the input data for the following blocks, and the forecast outputs are combined to generate the
 330 final prediction. Blocks are organized into stacks, with each stack dedicated to grasping specific data
 331 attributes using its own distinct set of functions. The network's input is a sequence of L lags (look-back
 332 period), with S stacks, each containing B blocks (Challu et al., 2022).

333 In each block, a *MaxPool* layer with varying kernel sizes (k_l) is employed at the input, enabling the block
 334 to focus on specific input components of different scales. Larger kernel sizes emphasize the analysis of
 335 larger-scale, low-frequency data, aiding in improving long-term forecasting accuracy. This approach,
 336 known as multi-rate signal sampling, alters the effective input signal sampling rate for each block's MLP
 337 (Challu et al., 2022).

338 Additionally, multi-rate processing has several advantages. It reduces memory usage, computational
 339 demands, and the number of learnable parameters, and helps prevent overfitting, while preserving the
 340 original receptive field. The following operation is applicable to the input $y_{t-L:t,l}$ of each block, with the
 341 first block ($l = 1$) using the network-wide input, where $y_{t-L:t,1} \equiv y_{t-L:t}$.

$$y_{t-L:t,l} = \text{MaxPool} (y_{t-L:t,l}, k_l) \quad (\text{Equation 15})$$

342 In many multi-horizon forecasting models, the number of neural network predictions matches the horizon's
 343 dimensionality, denoted as H . For instance, in N-BEATS, the number of predictions $|\theta_l^f| = H$. This results
 344 in a significant increase in computational demands and an unnecessary surge in model complexity as the
 345 horizon H becomes larger (Challu et al., 2022).

346 To address these challenges, N-HiTS proposes the use of temporal interpolation. This model manages the
 347 parameter counts per unit of output time ($|\theta_l^f| = [r_l H]$) by defining the dimensionality of the interpolation
 348 coefficients with respect to the expressiveness ratio r_l . To revert to the original sampling rate and predict
 349 all horizon points, this model employs temporal interpolation through the function g :

$$\hat{y}_{\tau,l} = g(\tau, \theta_l^f), \quad \forall \tau \in \{t + 1, \dots, t + H\}, \quad (\text{Equation 16})$$

$$\tilde{y}_{\tau,l} = g(\tau, \theta_l^b), \quad \forall \tau \in \{t-L, \dots, t\}, \quad (\text{Equation 17})$$

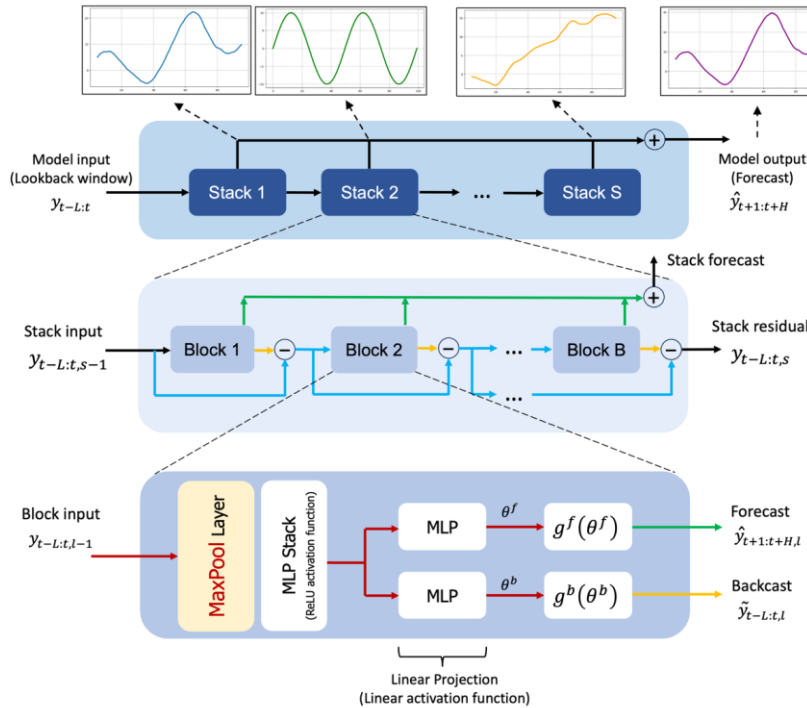
$$g(\tau, \theta) = \theta[t_1] + \left(\frac{\theta[t_2] - \theta[t_1]}{t_2 - t_1} \right) (\tau - t_1) \quad (\text{Equation 18})$$

$$t_1 = \arg \min_{t \in \tau: t \leq \tau} \tau - t, \quad t_2 = t_1 + 1/r_l \quad (\text{Equation 19})$$

350 The hierarchical interpolation approach involves distributing expressiveness ratios over blocks, integrated
 351 with multi-rate sampling. Blocks closer to the input employ more aggressive interpolation, generating lower
 352 granularity signals. These blocks specialize in analyzing more aggressively subsampled signals. The final
 353 hierarchical prediction, $\hat{y}_{t+1:t+H}$, is constructed by combining outputs from all blocks, creating
 354 interpolations at various time-scale hierarchy levels. This approach maintains a structured hierarchy of
 355 interpolation granularity, with each block focusing on its own input and output scales (Challu et al., 2022).
 356 To manage a diverse set of frequency bands while maintaining control over the number of parameters,
 357 exponentially increasing expressiveness ratios are recommended. As an alternative, each stack can be
 358 dedicated to modeling various recognizable cycles within the time series (e.g., weekly, or daily) employing
 359 matching r_l . Ultimately, the residual obtained from backcasting in the preceding hierarchy level is
 360 subtracted from the input of the subsequent level, intensifying the next-level block's attention on signals
 361 outside the previously addressed band (Challu et al., 2022).

$$\hat{y}_{t+1:t+H} = \sum_{l=1}^L \hat{y}_{t+1:t+H,l} \quad (\text{Equation 20})$$

$$y_{t-L:t,l+1} = y_{t-L:t,l} - \tilde{y}_{t-L:t,l} \quad (\text{Equation 21})$$



362

363 Figure 4. The structure of N-HiTS model programmed in this study. The architecture includes several
 364 Stacks, each Stack includes several Block, where each block consists of a MaxPool layer and a multi-
 365 layer which learns to produce coefficients for the backcast and forecast outputs of its basis.

366

367 2.3. Performance Metrics

368 To comprehensively evaluate the accuracy of flood predictions, we utilized a suite of metrics, including
 369 Nash-Sutcliffe Efficiency (NSE; Nash and Sutcliffe, 1970), persistent Nash-Sutcliffe Efficiency (persistent-
 370 NSE), Kling-Gupta efficiency (KGE; Gupta et al. 2009), Root Mean Square Error (RMSE), Mean
 371 Absolute Error (MAE), Peak Flow Error (PFE), and Time to Peak Error (TPE; Evin et al., 2023; Lobjegeois
 372 et al., 2014). These metrics collectively facilitate a rigorous assessment of the model's performance in
 373 reproducing the magnitude of observed peak flows and the shape of the hydrograph.

374 NSE measures the model's ability to explain the variance in observed data and assesses the goodness-of-fit
 375 by comparing the observed and simulated hydrographs. In hydrological studies, the NSE index is a widely
 376 accepted measure for evaluating the fitting quality of models (McCuen et al., 2006). It is calculated as:

$$NSE = 1 - \frac{\sum_{i=1}^n (Q_{s_i} - Q_{o_i})^2}{\sum_{i=1}^n (Q_{o_i} - \bar{Q}_o)^2} \quad (\text{Equation 22})$$

377 Where Q_{o_i} represents observed value at time i , Q_{s_i} represents simulated value at time i , \bar{Q}_o is the mean
 378 observed values and n is the number of data points. An NSE value of 1 indicates a perfect match between
 379 the observed and modeled data, while lower values represent the degree of departure from a perfect fit.

380 As the models are designed to predict one hour ahead in one of the prediction horizons, the persistent-NSE
 381 is essential for evaluating their performance. The standard NSE measures the model's sum of squared errors
 382 relative to the sum of squared errors when the mean observation is used as the forecast value. In contrast,
 383 persistent-NSE uses the most recent observed data as the forecast value for comparison (Nevo et al., 2022).
 384 The persistent NSE is calculated as:

$$persistent - NSE = 1 - \frac{\sum_{i=1}^n (Q_{s_i} - Q_{o_i})^2}{\sum_{i=1}^n (Q_{o_i} - Q_{o_{i-1}})^2} \quad (\text{Equation 23})$$

385 Where Q_{o_i} represents the observed value at time i , Q_{s_i} represents the simulated value at time i , $Q_{o_{i-1}}$ is the
 386 observed value at the last time step ($i - 1$) and n is the number of data points.

387 The KGE is a widely used performance metric in hydrological modeling and combines multiple aspects of
 388 model performance, including correlation, variability bias, and mean bias. The KGE metric is calculated
 389 using the following equation:

$$KGE = 1 - \sqrt{(r - 1)^2 + (\alpha - 1)^2 + (\beta - 1)^2} \quad (\text{Equation 24})$$

390 Where r represents Pearson correlation coefficient between observed Q_o and simulated Q_s values.
 391 α represents bias ratio, calculated as $\alpha = \frac{\mu_s}{\mu_o}$ where μ_s and μ_o are the means of simulated and observed data,
 392 respectively. β represents variability ratio, calculated as $\beta = \frac{\sigma_s/\mu_s}{\sigma_o/\mu_o}$ where σ_s and σ_o are the standard
 393 deviations of simulated and observed data, respectively.

394 RMSE quantifies the average magnitude of errors between observed and modeled values, offering insights
 395 into the absolute goodness-of-fit, while MAE is a measure of the average absolute difference between the
 396 modeled values and the observed values and provides a measure of the average magnitude of errors. RMSE
 397 is calculated as:

$$RMSE = \sqrt{\frac{1}{n} \sum_{i=1}^n (Q_{o_i} - Q_{s_i})^2} \quad (\text{Equation 25})$$

398 and MAE is calculated as:

$$MAE = \frac{1}{n} \sum_{i=1}^n |Q_{o_i} - Q_{s_i}| \quad (\text{Equation 26})$$

399 Where Q_{o_i} represents observed value at time i , Q_{s_i} represents simulated value at time i , and n is the number
400 of data points. RMSE and MAE provide information about the magnitude of modeling errors, with smaller
401 values indicating a better model fit.

402 PFE quantifies the magnitude disparity between observed and modeled peak flow values. The PFE metric
403 is defined as:

$$PFE = \frac{|Q_{o_{max}} - Q_{s_{max}}|}{Q_{o_{max}}} \quad (\text{Equation 27})$$

404 Where $Q_{o_{max}}$ represents the observed peak flow value, and $Q_{s_{max}}$ signifies the simulated peak flow value.
405 The PFE metric, expressed as a dimensionless value, provides a quantitative measure of the relative error
406 in predicting peak flow magnitudes concerning the observed values. A smaller PFE denotes more accurate
407 modeling of peak flow magnitudes, with a value of zero indicating a perfect match.

408 TPE assesses the temporal alignment of peak flows in the observed and modeled hydrographs. The TPE
409 metric is computed as:

$$TPE = |T_{o_{max}} - T_{s_{max}}| \quad (\text{Equation 28})$$

410 Where $T_{o_{max}}$ signifies the time at which the peak flow occurs in the observed hydrograph, and $T_{s_{max}}$
411 represents the time at which the peak flow occurs in the simulated hydrograph. TPE that is measured in
412 units of time (hours), provides insight into the precision of peak flow timing. Smaller TPE values indicate
413 a superior alignment between the observed and modeled peak flow timing, while larger TPE values indicate
414 discrepancies in the temporal occurrence of peak flows.

415 The utilization of these five metrics, PFE, persistent-NSE, TPE, NSE, and RMSE, collectively provides a
416 robust and multifaceted assessment of flood prediction performance. This approach ensures that both the
417 magnitude and timing of peak flows, as well as the overall hydrograph shape, are accurately calibrated and
418 validated.

419

420 **2.4. Sensitivity and Uncertainty Analysis**

421 When implementing NN models, it's crucial to understand how each input feature affects the model's
 422 performance or outputs. To achieve this, we systematically excluded each input feature from the model one
 423 by one (the Leave-One-Out method). For each exclusion, we retrained the model without that specific input
 424 feature and then tested its performance against a test dataset. This method helps in understanding which
 425 input features are most critical to the model's performance and which ones have a lesser impact. It also
 426 allows us to identify any input features that may be redundant or have little effect on the overall outcome,
 427 thus potentially simplifying the model without sacrificing accuracy.

428 In this study, we utilized probabilistic approaches to quantify the uncertainty in flood prediction. This
 429 method is rooted in statistical techniques employed for the estimation of unknown probability distributions,
 430 with a foundation in observed data. More specifically, we leveraged the Maximum Likelihood Estimation
 431 (MLE) approach, which entails the determination of MQL objective values that optimize the likelihood
 432 function. The likelihood function quantifies the probability of MQL objective taking values, given the
 433 observed realizations.

434 We incorporated the MQL as a probabilistic error metric into algorithmic architecture. MQL performs an
 435 evaluation by computing the average loss for a predefined set of quantiles. This computation is grounded
 436 in the absolute disparities between predicted quantiles and their corresponding observed values. By
 437 considering multiple quantile levels, MQL provides a comprehensive assessment of the model's ability to
 438 capture the distribution of the target variable, rather than focusing solely on point estimates.

439 The MQL metric also aligns closely with the Continuous Ranked Probability Score (CRPS), a standard tool
 440 for evaluating predictive distributions. CRPS measures the difference between the predicted cumulative
 441 distribution function and the observed values by integrating over all possible quantiles. The computation of
 442 CRPS involves a numerical integration technique that discretizes quantiles and applies a left Riemann
 443 approximation for CRPS integral computation. This process culminates in the averaging of these
 444 computations over uniformly spaced quantiles, providing a robust evaluation of the predictive distribution
 445 \hat{F}_t .

$$\text{MQL} (Q_\tau, [\hat{Q}_\tau^{q_1}, \dots, \hat{Q}_\tau^{q_i}]) = \frac{1}{n} \sum_{q_i} \text{QL} (Q_\tau, \hat{Q}_\tau^{q_i}) \quad (\text{Equation 29})$$

$$\text{CRPS} (Q_\tau, \hat{F}_t) = \int_0^1 \text{QL} (Q_\tau, \hat{Q}_\tau^{q_i}) dq \quad (\text{Equation 30})$$

$$\text{QL}(Q_\tau, \hat{Q}_\tau^q) = \frac{1}{H} \sum_{\tau=t+1}^{t+H} ((1-q)(\hat{Q}_\tau^q - Q_\tau) + q(Q_\tau - \hat{Q}_\tau^q)) \quad (\text{Equation 31})$$

446 Where Q_τ represents observed value at time τ , \hat{Q}_τ^q represents simulated value at time τ , q is the slope of the
 447 quantile loss, and H is the horizon of forecasting.

448 Implementation-wise, let $\mathcal{D} = \{(X_t, y_{t+h})\}_{t=1}^N$ denote training pairs, where X_t is the past 24-h discharge
 449 context and y_{t+h} the discharge h hours ahead. For a fixed horizon h and quantile levels $\{\tau_k\}_{k=1}^K$, each
 450 model f_θ outputs the vector of conditional quantiles:

$$\hat{\mathbf{Q}}_{t+h} = f_\theta(X_t) = (\hat{Q}_{t+h}^{\tau_1}, \dots, \hat{Q}_{t+h}^{\tau_K}) \in \mathbb{R}^K \quad (\text{Equation 32})$$

451 Parameters θ are learned by minimizing the multi-quantile (pinball) loss:

$$\mathcal{L}(\theta) = \frac{1}{NK} \sum_{t=1}^N \sum_{k=1}^K \rho_{\tau_k} (y_{t+h} - \hat{Q}_{t+h}^{\tau_k}), \quad (\text{Equation 33})$$

$$\rho_\tau(u) = \max(\tau u, (\tau - 1)u) = (\tau - \mathbb{1}_{\{u<0\}}) u$$

452 Because ρ_τ is convex and piecewise linear, its (sub)gradient with respect to $\hat{Q}_{t+h}^{\tau_k}$ is:

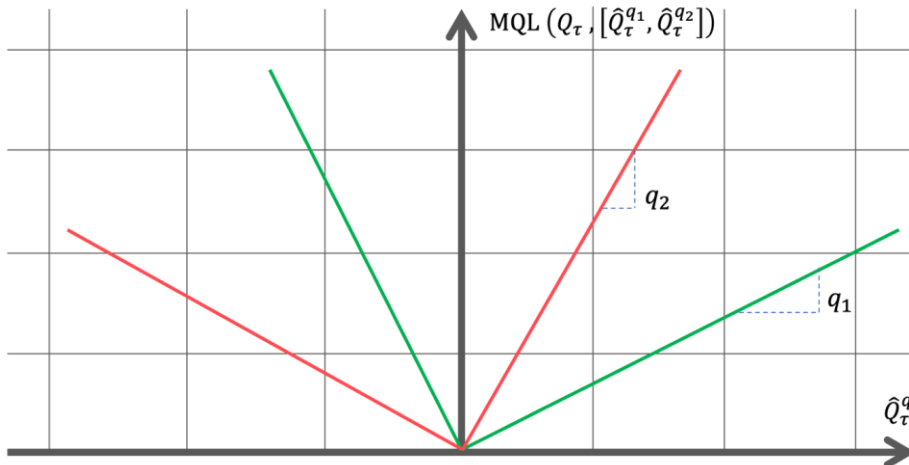
$$\frac{\partial \rho_\tau(y - \hat{Q}^\tau)}{\partial \hat{Q}^\tau} = \begin{cases} -(1-\tau), & y - \hat{Q}^\tau < 0, \\ -\tau, & y - \hat{Q}^\tau > 0, \end{cases} \quad (\text{Equation 34})$$

453 enabling backpropagation (Adam) without any sampling. Thus, each quantile $\hat{Q}_{t+h}^{\tau_k}$ is a direct network
 454 output learned to satisfy the quantile condition under ρ_τ . Uncertainty intervals are formed from these
 455 quantile predictions; for a 95% band we use $[\hat{Q}_{t+h}^{0.025}, \hat{Q}_{t+h}^{0.975}]$. The resulting bands quantify the uncertainty
 456 conditional on X_t .

457 To calculate the 95th PPU, we utilized the 0.95 quantile level within the MQL. This quantile level directly
 458 corresponds to the 95th percentile of the predicted distribution, providing an estimate of the 95% confidence
 459 interval. By examining the model's performance at this specific quantile, we effectively assessed its ability
 460 to accurately capture the predicted values with 95% confidence.

461 Incorporating MQL as a central metric in our study underscores its suitability for probabilistic forecasting,
 462 particularly in the context of uncertainty quantification. Unlike traditional error metrics that focus on point

463 predictions, MQL captures both central tendencies and variability by penalizing errors symmetrically across
 464 quantiles. This property ensures balanced and reliable assessments of the predictive distribution, ultimately
 465 enhancing the robustness and interpretability of flood prediction models.



466

467 Figure 5. The MQL function which shows loss values for different values of q when the true value is Q_τ .
 468 Furthermore, we employed two key indices, the R-Factor and the P-Factor, to rigorously assess the quality
 469 of uncertainty performance in our hydrological modeling. These metrics are instrumental in quantifying the
 470 extent to which the model's predictions encompass the observed data, thereby providing valuable insights
 471 into the model's predictive accuracy and reliability.

472 The P-Factor, or percentage of data within 95PPU, is the first index used in this assessment. The P-Factor
 473 quantifies the percentage of observed data that falls within the 95PPU, providing a measure of the model's
 474 predictive accuracy. The P-Factor can theoretically vary from 0% to a maximum of 100%. A P-Factor of
 475 100% signifies a perfect alignment between the model's predictions and the observed data within the
 476 uncertainty band. In contrast, a lower P-Factor indicates a reduced ability of the model to predict data within
 477 the specified uncertainty range.

$$P - Factor = \frac{Observations bracketed by 95PPU}{Number of observations} \times 100 \quad (\text{Equation } 3\underline{52})$$

478 The R-Factor can be computed by dividing the average width of the uncertainty band by the standard
 479 deviation of the measured variable. The R-Factor, with a minimum possible value of zero, provides a
 480 measure of the spread of uncertainty relative to the variability of the observed data. Theoretically, the R-

481 Factor spans from 0 to infinity, and a value of zero implies that the model's predictions precisely match the
482 measured data, with the uncertainty band being very narrow in relation to the variability of the observed
483 data.

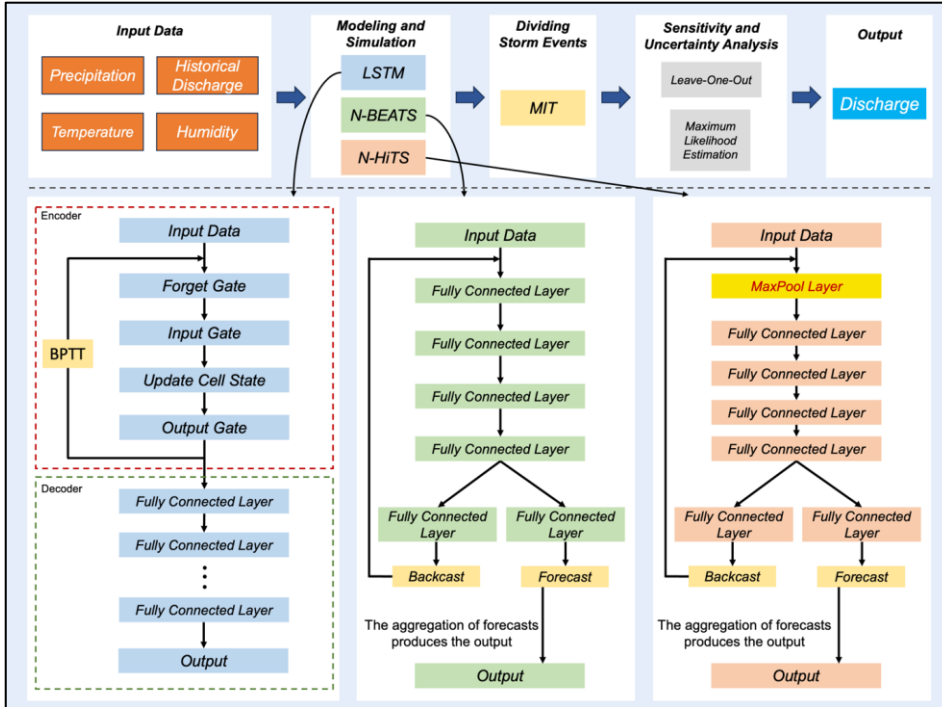
$$R - Factor = \frac{\text{Average width of 95PPU band}}{\text{Standard deviation of measured variables}} \times 100 \quad (\text{Equation 363})$$

484 In practice, the quality of the model is assessed by considering the 95% prediction band with the highest P-
485 Factor and the lowest R-Factor. This specific band encompasses most observed records, signifying the
486 model's ability to provide accurate and reliable predictions while effectively quantifying uncertainty. A
487 simulation with a P-Factor of 1 and an R-Factor of 0 signifies an ideal scenario where the model precisely
488 matches the measured data within the uncertainty band (Abbaspour et al., 2007).

489 Figure 6 shows the workflow of programming N-BEATS, N-HiTS, and LSTM for flood prediction. As
490 illustrated, the initial step involved cleaning and preparing the input data, which was then used to feed the
491 models. The workflow for each model and their output generation processes are depicted in Figure 6. We
492 segmented the storm events using the MIT approach, as previously described. Following this, we conducted
493 a sensitivity analysis using the Leave-One-Out method and performed uncertainty analysis using the MLE
494 approach to construct the 95PPU band. This rigorous methodology ensures a robust evaluation of model
495 performance under varying conditions and highlights the models' predictive reliability and resilience. We
496 employed the "NeuralForecast" Python package to develop the N-BEATS, N-HiTS, and LSTM models.
497 This package provides a diverse array of NN models with an emphasis on usability and robustness.

498

499



500

501 Figure 6. The workflow of N-BEATS, N-HiTS, and LSTM implementation. The upper section of the
 502 figure illustrates multiple steps from data preprocessing to model evaluation. The lower section provides a
 503 detailed view of the workflow and implementation for each model, highlighting the specific processes and
 504 methodologies employed in generating the outputs. Backpropagation Through Time (BPTT) trains LSTM
 505 by unrolling the model through time, computing gradients for each time step, and updating weights based
 506 on temporal dependencies.

507

508 **3. Results and Discussion**

509 **3.1. Independent Storms Delineation**

510 MIT's contextual delineation of storm events laid the groundwork for in-depth evaluation of rainfall events,
 511 enabling isolation and separation of rainfall events that led to significant flooding events. The nuanced
 512 outcomes of the MIT assessment contributed significantly to the understanding of rainfall variability and
 513 distribution as the dominant contributor to flood generation.

514 During modeling implementation, the initial imperative was the precise distinction of storm events within
515 the precipitation time series data of each case study. Our findings demonstrate that on average a dry period
516 of 7 hours serves as the optimal MIT time for both of our case studies. This outcome signifies that when a
517 dry interval of more than 7 hours transpires between two successive rainfall events, these subsequent
518 rainfalls should be considered two distinct storm events. This determination underlines the temporal
519 threshold necessary for distinguishing between individual meteorological phenomena in two case studies.

520

521 **3.2. Hyperparameter Optimization**

522 In the context of hyperparameter optimization, we systematically considered and tuned various
523 hyperparameters for the N-HiTS, N-BEATS, and LSTM. We searched for learning rates on a log-uniform
524 grid between 1×10^{-4} and 1×10^{-3} , batch sizes {16, 32, 64}, input size {1, 6, 12, 24} hours. For the
525 LSTM, recurrent layers {1,2,3}, hidden units per layer {64,128,256}, activation {tanh, ReLU}, decoder
526 MLP depth {1,2,3}, and decoder MLP width {64,128,256} were varied during the simulation run. For N-
527 HiTS, stacks {2,3,4}, blocks per stack {2,3,4,5}, block MLP width {64,128,256}, and block MLP depth
528 {2,3,4} were explored. For N-BEATS, we searched stacks {2,3,4}, blocks per stack {2,3,4,5}, block MLP
529 width {64,128,256}, and block MLP depth {2,3,4}; the interpretable (trend/seasonality) basis was kept
530 fixed. Following extensive exploration and fine-tuning of these hyperparameters, the optimal
531 configurations were identified (see Table 2). For the N-HiTS model, the most favorable outcomes were
532 achieved with the following hyperparameter settings: 2000 epochs, "identity" for scalar type, a learning rate
533 of 0.001, a batch size of 32, input size of 24 hours, "identity" for stack type, 512 units for hidden layers of
534 each stack, step size of 1, MQLoss as loss function, and "ReLU" for the activation function. As shown in
535 Table 2, the N-HiTS model demonstrated superior performance with 4 stacks, containing 2 blocks each,
536 and corresponding coefficients of 48, 24, 12, and 1, showcasing the significance of these settings for flood
537 prediction.

538 This hyperparameter optimization was also conducted for the N-BEATS model. In this model, we
539 considered 2000 epochs, 3 stacks with 2 blocks, "identity" for scalar type, a learning rate of 0.001, a batch
540 size of 32, input size of 24 hours, "identity" for stack type, 512 units for hidden layers of each stack, step
541 size of 1, MQLoss as loss function, and "ReLU" for the activation function.

542 Moreover, the LSTM as a benchmark model yielded its best results with 5000 epochs, an input size of 24
543 hours, "identity" as the scalar type, a learning rate of 0.001, a batch size of 32, and "tanh" as the activation
544 function. Furthermore, LSTM's hidden state was most effective with two layers containing 128 units, and
545 the MLP decoder thrived with two layers encompassing 128 units. These meticulously optimized

546 hyperparameter settings represent the culmination of efforts to ensure that each model operates at its peak
547 potential, facilitating accurate flood prediction.

548 Table 2. Optimized values for the hyperparameters.

Hyperparameter	N-HiTS	N-BEATS	LSTM
Epoch	2000	2000	5000
Scaler type	identity	identity	standard
Learning rate	0.001	0.001	0.001
Batch size	32	32	32
Input size	24 hours	24 hours	24 hours
Stack type	Seasonality, trend, identity, identity	Seasonality, trend, identity	*
Number of units in each hidden layer	512	512	128
Loss function	MQLoss	MQLoss	MQLoss
Activation function	ReLU	ReLU	tanh
Number of stacks	4	3	*
Number of blocks in each stack	2	2	*
Stacks' coefficients	48,24,12,1	*	*

549 *Not applicable

550 In Table 2, "epoch" refers to the number of training steps, and "scaler type" indicates the type of scaler used
551 for normalizing temporal inputs. The "learning rate" specifies the step size at each iteration while optimizing
552 the model, and the "batch size" represents the number of samples processed in one forward and backward
553 pass. The "loss function" quantifies the difference between the predicted outputs and the actual target
554 values, while the "activation function" determines whether a neuron should be activated. The "stacks'
555 coefficients" in the N-HITS model control the frequency specialization for each stack, enabling effective
556 handling of different frequency components in the time series data.

557 Another hyperparameter for all three models is input size, which is a variable that determines the maximum
558 sequence length for truncated backpropagation during training and the number of autoregressive inputs
559 (lags) that the models considered for prediction. Essentially, input size represents the length of the historical
560 series data used as input to the model. This variable offers flexibility in the models, allowing them to learn
561 from a defined window of past observations, which can range from the entire historical dataset to a subset,

562 tailored to the specific requirements of the prediction task. In the context of flood prediction, determining
563 the appropriate input size is crucial to adequately capture the meteorological data preceding the flood event.
564 To address this, we calculated the time of concentration (TC) of the watershed system and set the input size
565 to exceed this duration. According to the Natural Resources Conservation Service (NRCS), for typical
566 natural watershed conditions, the TC can be calculated from lag time, the time between peak rainfall and
567 peak discharge, using the formula: $Lag\ time = TC \times 0.6$ (NRCS, 2009). Specifically, the average TC in
568 the Lower Dog River watershed and Upper Dutchmans Creek watershed was found to be 19 and 22 hours,
569 respectively. As these represent the average TC for our case studies, we selected the 24 hours for input data,
570 slightly longer than the average TC , ensuring sufficient coverage of relevant meteorological data preceding
571 all flood events.

572

573 **3.3. Flood Prediction and Performance Assessment**

574 In this study, we conducted a comprehensive performance evaluation of N-HiTS, N-BEATS, and
575 benchmarked these models with LSTM, utilizing two case studies: the Lower Dog River and the Upper
576 Dutchmans Creek watersheds. Within these case studies, we trained and validated the models separately
577 for each watershed across a diverse set of storm events from 01/10/2007 to 01/10/2022 (15 years) in the
578 Lower Dog River and from 21/12/1994 to 01/10/2022 (27 years) in the Upper Dutchmans Creek. The
579 decision to train separate models for each catchment was made to account for the unique hydrological
580 characteristics and local features specific to each watershed. By training models individually, we aimed to
581 optimize performance by tailoring each model to the distinct rainfall-runoff relationship inherent in each
582 catchment. All algorithms were tested using unseen flooding events that occurred between 14/12/2022 and
583 28/03/2023. Our targets were event-focused, where operational value focuses on performance during rising
584 limbs, peaks, and recessions. Evaluating over the entire continuous hydrograph (testing period) can dilute
585 or even mask differences. For this reason, we prioritized an event-centric assessment as the primary
586 evaluation approach rather than full-period metrics. In the Dog River gauging station, two winter storms,
587 i.e., January 3rd to January 5th, 2023 (Event 1) and February 17th to February 18th, 2023 (Event 2), as well
588 as a spring flood event that occurred during March 26th to March 28th, 2023 (Event 3) were selected for
589 testing. Additionally, three winter flooding events, i.e., December 14th to December 16th, 2022 (Event 4),
590 January 25th and January 26th, 2023 (Event 5), and February 11th to February 13th, 2023 (Event 6), were
591 chosen to test the algorithms across the Killian Creek gauging station in the Upper Dutchmans Creek. The
592 rainfall events corresponding to these flooding events were delineated using the MIT technique discussed
593 in Section 3.1.

594 Our results for the Lower Dog River case study explicitly demonstrated the accuracy of both N-HiTS and
595 N-BEATS in generating the winter and spring flood hydrographs compared to the LSTM model across all
596 selected storm events. Although, N-HiTS prediction slightly outperformed N-BEATS during winter
597 prediction (January 3rd to January 5th, 2023). In this event, N-HiTS outperformed N-BEATS with a
598 difference of 11.6% in MAE and 20% in RMSE. The N-HiTS slight outperformance (see Tables 3 and 4)
599 is attributed to its unique structure that allows the model to discern and capture intricate patterns within the
600 data. Specifically, N-HiTS predicted flooding events hierarchically using blocks specialized in different
601 rainfall frequencies based on controlled signal projections, through expressiveness ratios, and interpolation
602 of each block. The coefficients are then used to synthesize backcast through
603 $\tilde{y}_t - L: t, l$ and forecast $(\tilde{y}_{t+1}: t + H, l)$ outputs of the block as a flood value. The coefficients were locally
604 determined along the horizon, allowing N-HiTS to reconstruct nonstationary signals over time.

605 While the N-HiTS emerged as the most accurate in predicting flood hydrograph among the three models,
606 its performance was somehow comparable with N-BEATS. The N-BEATS model exhibited good
607 performance in two case studies. It consistently provided competitive results, demonstrating its capacity to
608 effectively handle diverse storm events and deliver reliable predictions. N-BEATS has a generic and
609 interpretable architecture depending on the blocks it uses. Interpretable configuration sequentially projects
610 the signal into polynomials and harmonic basis to learn trend and seasonality components while generic
611 configuration substitutes the polynomial and harmonic basis for identity basis and larger network's depth.
612 In this study, we used interpretable architecture, as it regularizes its predictions through projections into
613 harmonic and trend basis that is well-suited for flood prediction tasks. Using interpretable architecture,
614 flood prediction was aggregated in a hierarchical fashion. This enabled the building of a very deep neural
615 network with interpretable flood prediction outputs.

616 It is essential to underscore that, despite its strong performance, the N-BEATS model did not surpass the
617 N-HiTS model in terms of NSE, Persistent-NSE, MAE, and RMSE for the Lower Dog River case study.
618 Although both models showed almost the same KGE values. Notably, the N-BEATS model showcased
619 superior results based on the PFE metric, signifying its exceptional capability in accurately predicting flood
620 peaks. However, both N-HiTS and N-BEATS models overestimated the flood peak rate of Event 2 for the
621 Lower Dog River watershed. This event, which occurred from February 17th to February 18th, 2023, was
622 flashy, short, and intense proceeded by a prior small rainfall event (from February 12th until February 13th)
623 that minimized the rate of infiltration. This flash flood event caused by excessive rainfall in a short period
624 of time (<8 hours) was challenging to predict for N-BEATS and N-HiTS models. In addition, predicting
625 the magnitude of changes in the recession curve of the third event seems to be a challenge for both models.
626 The specific part of the flood hydrograph after the precipitation event, where flood diminishes during a

rainless is dominated by the release of runoff from shallow aquifer systems or natural storages. It seems both models showed a slight deficiency in capturing this portion of the hydrograph when the rainfall amount decreases over time in the Dog River gauging station.

Conversely, in the Killian Creek gauging station, the N-BEATS model almost emerged as the top performer in predicting the flood hydrograph based on NSE, Persistent-NSE, RMSE, and PFE performance metrics (see Tables 3 and 4). KGE values remained almost the same for both models. In addition, both N-BEATS and N-HiTS slightly overpredicted time to peak values for Event 5. This reflects the fact that when rainfall varies randomly around zero, it provides less to no information for the algorithms to learn the fluctuations and patterns in time series data. Both N-HiTS and N-BEATS provided comparable results for all events predicted in this study. N-HiTS builds upon N-BEATS by adding a MaxPool layer at each block. Each block consists of an MLP layer that learns how to produce coefficients for the backcast and forecast outputs. This subsamples the time series and allows each stack to focus on either short-term or long-term effects, depending on the pooling kernel size. Then, the partial predictions of each stack are combined using hierarchical interpolation. This ability enhances N-HiTS capabilities to produce drastically improved, interpretable, and computationally efficient long-horizon flood predictions.

In contrast, the performance of LSTM as a benchmark model lagged behind both N-HiTS and N-BEATS models for all events across two case studies. Despite its extensive applications in various hydrology domains, the LSTM model exhibited comparatively lower accuracy when tasked with predicting flood responses during different storm events. Focusing on NSE, Persistent-NSE, KGE, MAE, RMSE, and PFE metrics, it is noteworthy that all three models, across both case studies, consistently succeeded in capturing peak flow rates at the appropriate timing. All models demonstrated commendable results with respect to the TPE metric. In most scenarios, TPE revealed a value of 0, signifying that the models accurately pinpointed the peak flow rate precisely at the expected time. In some instances, TPE reached a value of 1, showing a deviation of one hour in predicting the peak flow time. This deviation is deemed acceptable, particularly considering the utilization of short, intense rainfall for our analysis.

Our investigation into the performance of the three distinct forecasting models yielded compelling results pertaining to their ability to generate 95PPU, as quantified by the P-Factor and R-Factor. These factors serve as critical indicators for assessing the reliability and precision of the uncertainty bands produced by the MLE. Our findings demonstrated that the N-HiTS and N-BEATS models outperformed the LSTM model in mathematically defining uncertainty bands, in terms of R-Factor metric. The R-Factor, a crucial metric for evaluating the average width of the uncertainty band, consistently favored the N-HiTS and N-BEATS models over their counterparts. This finding was consistent across a diverse range of storm events. In addition, coupling MLE with the N-HiTS and N-BEATS models demonstrated superior performance in

660 generating 95PPU when assessed through the P-Factor metric. The P-Factor represents another vital aspect
661 of uncertainty quantification, focusing on the precision of the uncertainty bands.

662 Figures 7 and 8 present graphical depictions of the predicted flood with 1-hour prediction horizon and
663 uncertainty assessment for each model as well as Flow Duration Curve (FDC) across two gauging
664 stations. As illustrated, the uncertainty bands skillfully bracketed most of the observational data, reflecting
665 the fact that MLE was successful in reducing errors in flood prediction. FDC analysis also revealed that N-
666 HiTS and N-BEATS models skillfully predicted the flood hydrograph, however, both models were
667 particularly successful in predicting moderate to high flood events (1800-6000 and >6000 cfs). In the FDC
668 plots, the x-axis denotes the exceedance probability, expressed as a percentage, while the y-axis signifies
669 flood in cubic feet per second. Notably, these plots reveal distinctive patterns in the performance of the N-
670 HiTS, N-BEATS, and LSTM models.

671 Within the lower exceedance probability range, particularly around the peak flow, the N-HiTS and N-
672 BEATS models demonstrated a clear superiority over the LSTM model, closely aligning with the observed
673 data. This observed trend is consistent when examining the corresponding hydrographs. Across all events,
674 the flood hydrographs generated by N-HiTS and N-BEATS exhibited a closer resemblance to the observed
675 data, particularly in the vicinity of the peak timing and rate, compared to the hydrographs produced by the
676 LSTM model. These findings underscore the enhanced predictive accuracy and reliability of the N-HiTS
677 and N-BEATS models, particularly in predicting moderate to high flood events as well as critical
678 hydrograph features such as peak flow rate and timing. The alignment of model-generated FDCs and
679 hydrographs with observed data in the proximity of peak flow further establishes the efficiency of N-HiTS
680 and N-BEATS in accurately reproducing the dynamics of flood generation mechanisms across two
681 headwater streams.

682 Table 3. The performance metrics for the Lower Dog River flood predictions with 1-hour prediction
683 horizon.

Model	Performance Metric	Event 1	Event 2	Event 3
N-HiTS	NSE	0.995	0.991	0.992
	Persistent-NSE	0.947	0.931	0.948
	KGE	0.977	0.989	0.976
	RMSE	123.2	27.6	68.5
	MAE	64.1	12.0	37.8
	PFE	0.018	0.051	0.015
TPE (hours)		0	1	0

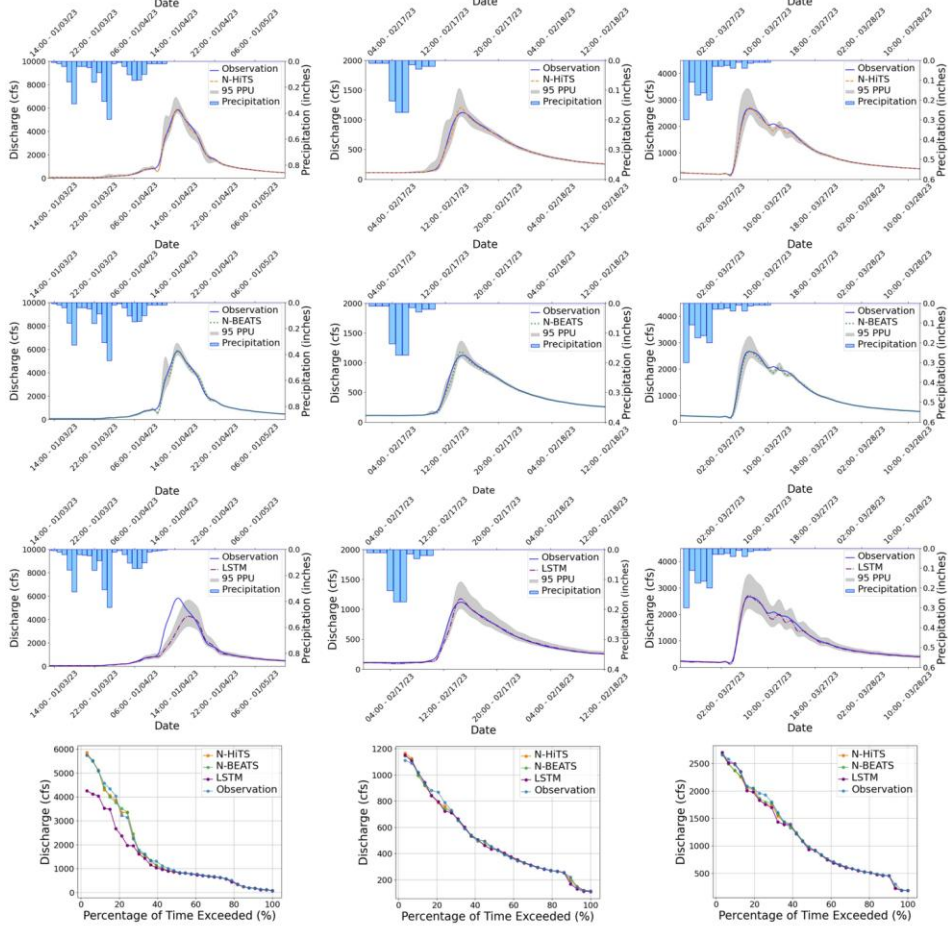
	P-Factor	96.9 %	100 %	93.5 %
	R-Factor	0.27	0.40	0.33
	NSE	0.991	0.989	0.993
	Persistent-NSE	0.917	0.916	0.956
	KGE	0.984	0.984	0.98
	RMSE	154.1	30.5	62.5
N-BEATS	MAE	72.6	13.6	35.9
	PFE	0.0005	0.031	0.0002
	TPE (hours)	0	1	0
	P-Factor	87.8 %	100 %	90.3 %
	R-Factor	0.17	0.23	0.24
	NSE	0.756	0.983	0.988
	Persistent-NSE	-1.44	0.871	0.929
	KGE	0.765	0.978	0.971
	RMSE	841.1	37.9	79.5
LSTM	MAE	369.4	18.6	42
	PFE	0.258	0.036	0.016
	TPE (hours)	1	0	0
	P-Factor	81.8 %	93.1 %	96.7 %
	R-Factor	0.37	0.51	0.6

684

685 Table 4. The performance metrics for the Killian Creek flood predictions with 1-hour prediction horizon.

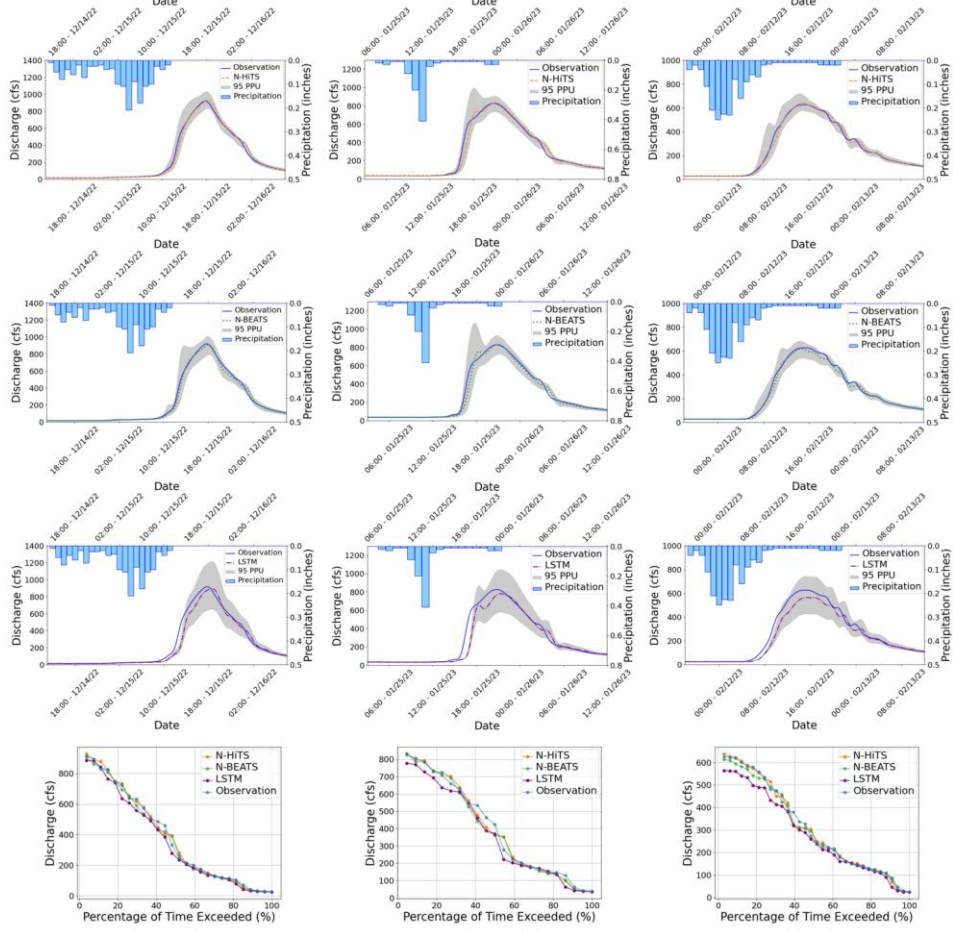
Model	Performance Metric	Event 4	Event 5	Event 6
	NSE	0.991	0.971	0.991
	Persistent-NSE	0.885	0.806	0.844
	KGE	0.982	0.967	0.991
	RMSE	28.8	46.0	19.0
N-HITS	MAE	17.9	23.8	11.5
	PFE	0.017	0.008	0.020
	TPE (hours)	0	0	0
	P-Factor	92.6 %	90.9 %	100 %
	R-Factor	0.39	0.48	0.45

	NSE	0.992	0.973	0.989
	Persistent-NSE	0.908	0.821	0.823
	KGE	0.972	0.951	0.973
	RMSE	25.7	44.2	20.2
N-BEATS	MAE	18.3	25.9	14.0
	PFE	0.006	0.008	0.019
	TPE (hours)	0	0	0
	P-Factor	96.3 %	86.3 %	96.9 %
	R-Factor	0.43	0.53	0.43
	NSE	0.952	0.892	0.935
	Persistent-NSE	0.4	0.27	0.087
LSTM	KGE	0.92	0.899	0.901
	RMSE	65.7	89.2	50.3
	MAE	41.1	45	35.9
	PFE	0.031	0.058	0.098
	TPE (hours)	1	0	0
	P-Factor	70.4 %	72.73 %	81.82 %
	R-Factor	0.66	0.7	0.65



687

688 Figure 7. 95 PPU band and FDC plots of N-HiTS, N-BEATS, and LSTM models with 1-hour prediction
689 horizon for the three selected flooding events in the Lower Dog River gauging station.



690 **Event 4**

691 **Event 5**

692 **Event 6**

693 Figure 8. 95 PPU band and FDC plots of N-HiTS, N-BEATS, and LSTM models with 1-hour prediction
 694 horizon for the three selected flooding events in the Killian Creek gauging station.

695 To evaluate robustness across lead times, we extended the analysis to 3- and 6-hour prediction horizons.
 696 The results are presented in Figures 9-12, and Tables 5 and 6. As expected, NSE and KGE decreased while
 697 the absolute errors increased with horizon for all models; however, N-HiTS and N-BEATS continued to
 698 outperform LSTM across both stations and events. At Killian Creek station, both N-HiTS and N-BEATS
 699 preserved their lead, yielding higher NSE and lower MAE/RMSE than LSTM, while at the Lower Dog
 700 River, N-BEATS remained slightly superior on the same metrics. KGE values stayed comparable between

699 the two feed-forward models, and peak-focused metrics (PFE and TPE) indicated that both still captured
 700 peak magnitude and timing reliably, compared to LSTM. Uncertainty bands widened with horizon as
 701 expected, but the likelihood-based 95PPU for N-HiTS and N-BEATS maintained tighter R-Factors and
 702 competitive P-Factors relative to LSTM, especially around moderate-to-high flows. Flow-duration
 703 diagnostics at multi-hour leads reinforced these findings, showing closer alignment of N-HiTS and N-
 704 BEATS to observations in the upper tail. Overall, the multi-horizon results corroborate the 1-hour horizon
 705 results: N-HiTS and N-BEATS deliver more accurate and reliable flood forecasts than LSTM, and their
 706 relative strengths persist at 3 and 6 hours ahead. For completeness, we also evaluated 12- and 24-hour lead
 707 times. During these horizons, all models' performances declined sharply (NSE < 0.4 across sites and
 708 events), so we restrict detailed reporting to 1–6 hours where performance remains operationally meaningful.

709 Table 5. The performance metrics of the models with 3-hour prediction horizon.

Model	Performance Metric	Event 1	Event 2	Event 3	Event 4	Event 5	Event 6
N-HiTS	NSE	0.91	0.86	0.58	0.83	0.81	0.89
	KGE	0.92	0.92	0.74	0.85	0.85	0.88
	RMSE	506	107	485	122	119	65
	MAE	293	58	209	71	65	42
	PFE	0.03	0.02	0.08	0.1	0.07	0.05
	TPE (hours)	0	0	0	0	0	0
	P-Factor	97 %	100 %	93.5 %	85 %	72 %	88 %
N-BEATS	R-Factor	0.8	1.3	0.75	0.99	0.92	1.14
	NSE	0.92	0.88	0.56	0.82	0.82	0.89
	KGE	0.91	0.91	0.72	0.83	0.84	0.87
	RMSE	481	101	498	124	115	63
	MAE	241	48	207	67	58	33
	PFE	0.04	0.02	0.12	0.006	0.02	0.002
	TPE (hours)	1	0	2	0	0	0
	P-Factor	90.9 %	93 %	90.3 %	92 %	68 %	94 %

	R-Factor	0.7	1.2	0.74	0.78	1.1	0.87
LSTM	NSE	0.7	0.77	0.42	0.82	0.51	0.55
	KGE	0.765	0.87	0.65	0.79	0.64	0.69
	RMSE	928	139	575	125	190	133
	MAE	487	80	296	85	118	87
	PFE	0.12	0.03	0.16	0.16	0.44	0.08
	TPE (hours)	2	1	2	2	1	2
	P-Factor	75.8 %	96 %	83.9 %	100 %	90 %	94 %
	R-Factor	1.15	1.88	1.66	2.8	3.7	2.4

710

711

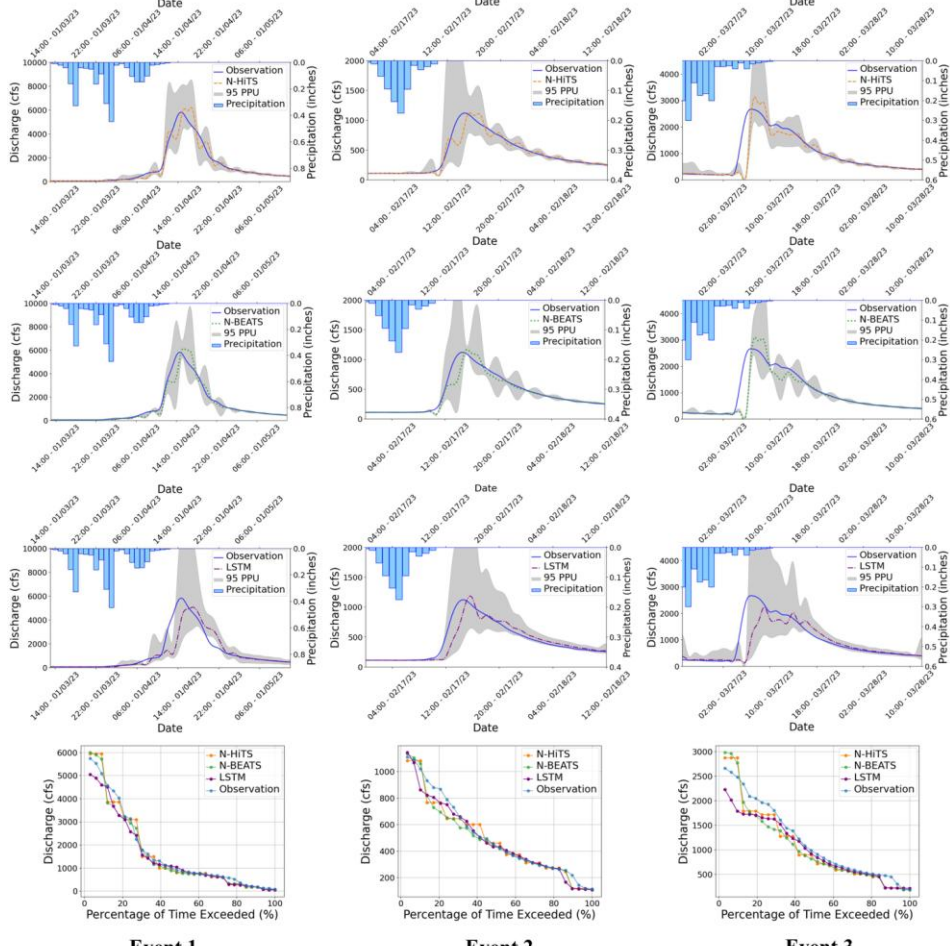
Table 6. The performance metrics of the models with 6-hour prediction horizon.

Model	Performance Metric	Event 1	Event 2	Event 3	Event 4	Event 5	Event 6
N-HiTS	NSE	0.82	0.58	0.51	0.6	0.7	0.52
	KGE	0.76	0.68	0.67	0.74	0.78	0.67
	RMSE	708	189	525	188	147	137
	MAE	423	90	257	110	90	77
	PFE	0.35	0.29	0.12	0.03	0.2	0.1
	TPE (hours)	2	3	0	0	3	3
	P-Factor	70 %	96 %	87 %	92 %	82 %	87 %
	R-Factor	0.71	1.1	1.1	1.8	1.15	1.2
N-BEATS	NSE	0.94	0.85	0.59	0.33	0.82	0.59
	KGE	0.83	0.82	0.73	0.55	0.79	0.67
	RMSE	386	112	481	244	115	126
	MAE	259	58	181	131	56	74

	PFE	0.16	0.23	0.02	0.03	0.03	0.12
	TPE (hours)	0	3	0	0	0	3
	P-Factor	100 %	86 %	90.3 %	85 %	77 %	78 %
	R-Factor	1.8	2.3	1.1	1.13	3.3	1.2
LSTM	NSE	- 0.35	- 0.39	- 0.22	- 0.17	- 0.2	- 0.2
	KGE	0.3	0.05	0.18	0.34	0.33	0.4
	RMSE	1984	348	834	324	300	220
	MAE	1304	192	468	234	201	174
	PFE	0.24	0.36	0.42	0.6	0.44	0.42
	TPE (hours)	3	4	3	0	2	2
	P-Factor	36 %	79 %	90.3 %	85 %	86 %	63 %
	R-Factor	1.8	1.9	2.16	1.6	3.7	1.6

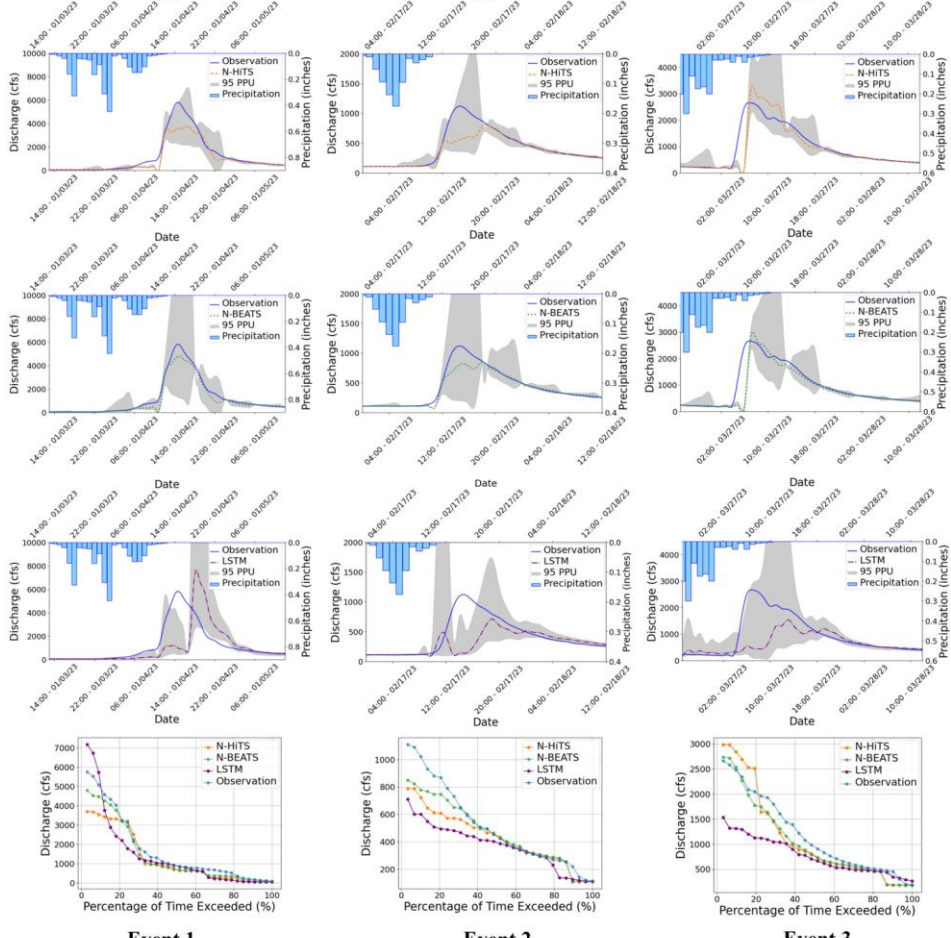
712

713



714

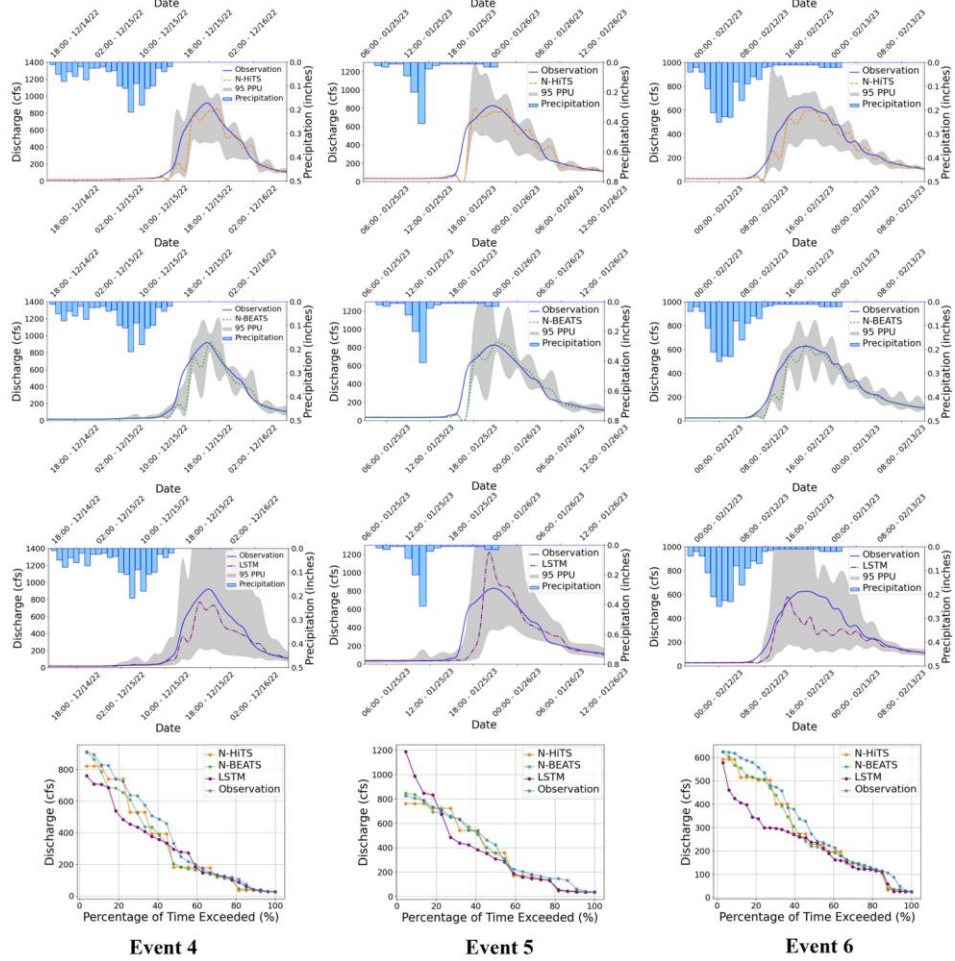
715 Figure 9. 95 PPU band and FDC plots of N-HiTS, N-BEATS, and LSTM models with 3-hour prediction
 716 horizon for the three selected flooding events in the Lower Dog River gauging station.



717

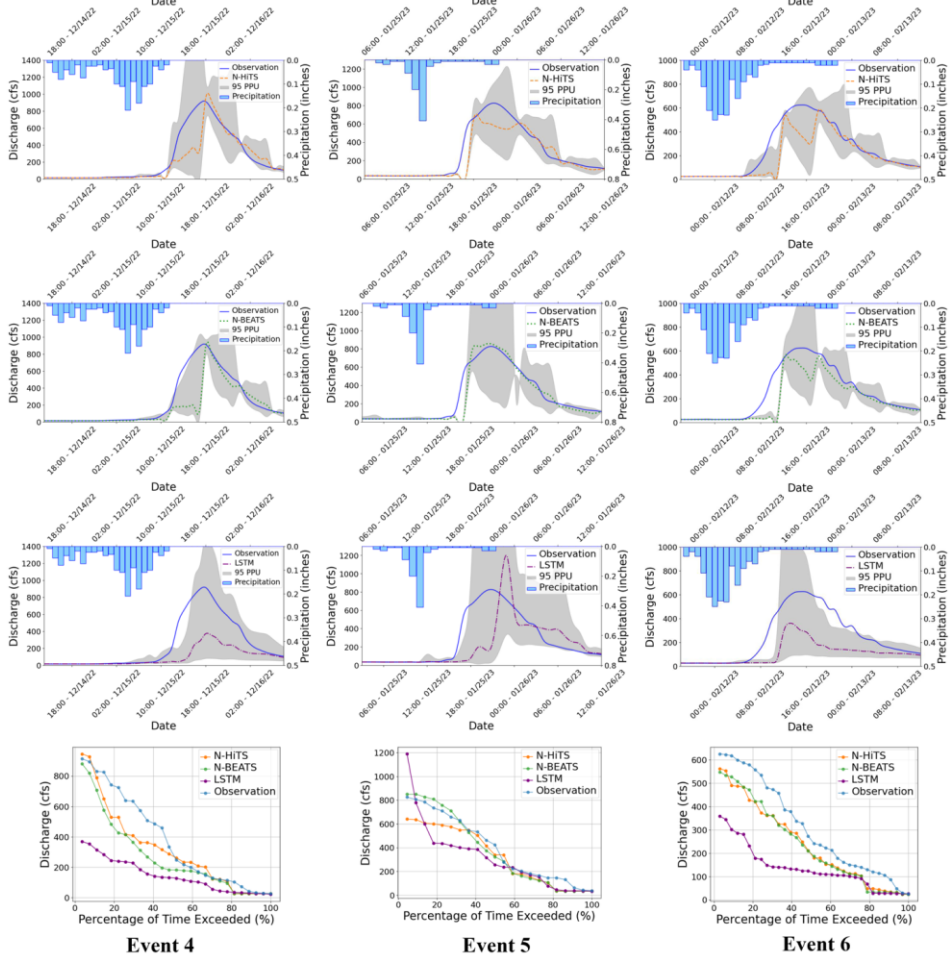
718 Figure 10. 95 PPU band and FDC plots of N-HiTS, N-BEATS, and LSTM models with 6-hour prediction
 719 horizon for the three selected flooding events in the Lower Dog River gauging station.

720



721

722 Figure 11. 95 PPU band and FDC plots of N-HiTS, N-BEATS, and LSTM models with 3-hour prediction
723 horizon for the three selected flooding events in the Killian Creek gauging station.



724

725 Figure 12. 95 PPU band and FDC plots of N-HiTS, N-BEATS, and LSTM models with 6-hour prediction
 726 horizon for the three selected flooding events in the Killian Creek gauging station.

727 To probe cross-catchment generalizability, we trained a single “regional” model by pooling Lower Dog
 728 River and Killian Creek, preserving per-site temporal splits and fitting a global scaler only on the pooled
 729 training portion to avoid leakage; evaluation remained strictly per site. Relative to per-site training, pooled
 730 fitting produced a small accuracy drop for N-HiTS and N-BEATS (~ 2 to 3 %). LSTM showed mixed
 731 performance to pooling, it improved in some storm events but degraded in others, so that, when averaged
 732 across both stations and storm events, LSTM’s regional performance was effectively unchanged relative to

733 the per-site training. Despite that, the regional N-HiTS/N-BEATS matched the accuracy of the best per-site
734 models within the variability observed across storm events and, importantly, consistently surpassed LSTM
735 at both basins. Mechanistically, N-HiTS's multi-rate pooling and hierarchical interpolation, and N-
736 BEATS's trend/seasonality basis projection, act as catchment-invariant feature extractors that support
737 parameter sharing across stations.

738 In our investigation, we conducted an analysis to assess the impact of varying input sizes on the performance
739 of the N-HiTS, as the best model. We implemented four different durations as input sizes to observe the
740 corresponding differences in modeling performance. Notably, one of the key metrics affected by changes
741 in input size was 95PPU, which exhibited a general decrease with increasing input size. As detailed in Table
742 7, we observed a discernible trend in the R-Factor of the N-HiTS model as the input size was increased.
743 Specifically, there was a decline in the R-Factor as the input size expanded. This trend underscores the
744 influence of input size on model performance, particularly in terms of 95PPU band and accuracy.

745 Overall, uncertainty analysis revealed that coupling MLE with N-HiTS and N-BEATS models
746 demonstrated superior performance in generating 95PPU, effectively reducing errors in flood prediction.
747 The MLE approach was more successful in reducing 95PPU bands of N-HiTS and N-BEATS models
748 compared to the LSTM, as indicated by the R-Factor and P-Factor. The N-BEATS model demonstrated a
749 narrower uncertainty band (lower R-Factor value), while the N-HiTS model provided higher precision.
750 Furthermore, incorporating data with various sizes into the N-HiTS model led to a narrower 95PPU and an
751 improvement in the R-Factor, highlighting the significance of input size in enhancing model accuracy and
752 reducing uncertainty.

Table 7. N-HiTS's R-Factor results for three storm events in each case study, using 1
hour, 6 hours, 12 hours, and 24 hours input size in training.

Input Size	1 hour	6 hours	12 hours	24 hours
Dog River, GA - Event 1	0.314	0.337	0.29	0.272
Dog River, GA - Event 2	0.35	0.413	0.403	0.402
Dog River, GA - Event 3	0.358	0.459	0.374	0.336
Killian Creek, NC - Event 4	0.491	0.422	0.426	0.388
Killian Creek, NC - Event 5	0.584	0.503	0.557	0.483
Killian Creek, NC - Event 6	0.482	0.42	0.446	0.454

753

754 **3.4. Sensitivity Analysis**

755 In this study, we conducted a comprehensive sensitivity analysis of the N-HiTS, N-BEATS, and LSTM
756 models to evaluate their responsiveness to meteorological variables, specifically precipitation, humidity,
757 and temperature. The goal was to assess how the omission of input features impacts the overall modeling
758 performance compared to their full-variable counterparts.

759 To execute this analysis, we systematically trained each model by excluding meteorological variables one
760 or more at a time, subsequently evaluating their predictive performance using the entire testing dataset.
761 The results of our analysis indicated that N-HiTS and N-BEATS models exhibited minimal sensitivity to
762 meteorological variables, as evidenced by the negligible impact on their performance metric (i.e., NSE,
763 Persistent-NSE, KGE, RMSE, and MAE) upon input feature exclusion.

764 Notably, as shown in Table 8, the performance of the N-HiTS model displayed a marginal deviation
765 under variable omission, while the N-BEATS model exhibited consistent performance irrespective of the
766 inclusion or exclusion of meteorological variables. The structure of this algorithm is based on backward
767 and forward residual links for univariate time series point forecasting which does not take into account
768 other input features in the prediction task. These findings suggest that the predictive capabilities of N-
769 HiTS and N-BEATS models predominantly rely on historical flood data. Both models demonstrated
770 strong performance even without incorporating precipitation, temperature, or humidity data, underscoring
771 their ability in flood prediction in the absence of specific meteorological inputs. This capability
772 underscores the robustness of the N-HiTS and N-BEATS models, positioning them as viable tools and
773 perhaps appropriate for real-time flood forecasting tasks where direct meteorological data may be limited
774 or unavailable.

775 Table 8. Performance metrics' values for N-HiTS, N-BEATS, and LSTM models by excluding
776 meteorological variables one or more at a time.

Model	Excluded Variables	NSE	Persistent-NSE	KGE	RMSE	MAE
N-HiTS	Using all variables	0.996	0.92	0.988	22.66	4.19
	Without Precipitation	0.993	0.91	0.97	23.28	4.31
	Without Humidity	0.995	0.914	0.976	22.87	4.22
	Without Temperature	0.995	0.921	0.985	22.43	4.14

	Discharge only prediction	0.993	0.911	0.972	23.21	4.29
	Using all variables	0.994	0.978	0.992	11.80	2.13
	Without Precipitation	0.994	0.978	0.991	11.86	2.17
N-BEATS	Without Humidity	0.994	0.978	0.991	11.81	2.16
	Without Temperature	0.994	0.978	0.991	11.82	2.16
	Discharge only prediction	0.994	0.978	0.991	11.96	2.17
LSTM	Using all variables	0.992	0.865	0.926	29.52	8.15
	Without Precipitation	0.979	0.665	0.892	39.46	19.83
	Without Humidity	0.991	0.843	0.925	31.73	9.15
	Without Temperature	0.983	0.628	0.872	48.95	11.49
	Discharge only prediction	0.976	0.576	0.692	52.28	33.5

777

778 **3.5 Computational Efficiency**

779 The computational efficiency of the N-HiTS, N-BEATS, and LSTM models, as well as a comparative
 780 analysis, is presented in Table 9. The study encompassed the entire process of training and predicting over
 781 the testing period, employing the optimized hyperparameters as previously described. Regarding the
 782 training time, it is noteworthy that the LSTM model exhibited the quickest performance. Specifically,
 783 LSTM demonstrated a training time that was 71% faster than N-HiTS and 93% faster than N-BEATS in
 784 the Lower Dog River watershed, while it was respectively, 126% and 118% faster than N-HiTS and N-
 785 BEATS in the Upper Dutchmans Creek, over training dataset. This is because LSTM has simple
 786 architecture compared to the N-BEATS and N-HiTS and does not require multivariate features, hierarchical
 787 interpolation, and multi-rate data sampling. Perhaps, this outcome underscores the computational advantage
 788 of LSTM over other algorithms.

789 Conversely, during the testing period, the N-HiTS model emerged as the fastest and delivered the most
 790 efficient results in comparison to the other models. Notably, N-HiTS displayed a predicted time that was

791 33% faster than LSTM and 32% faster than N-BEATS. This finding highlights the computational efficiency
792 of the N-HiTS model in the context of predicting processes. Our experiments unveiled an interesting
793 contrast in the computational performance of these models. While LSTM excelled in terms of training time,
794 it lagged behind when it came to the testing period.

795 In the grand scheme of computational efficiency, model accuracy, and uncertainty analysis results, it
796 becomes evident that the superiority of the N-HiTS and N-BEATS models in terms of accuracy and
797 uncertainty analysis holds paramount importance. This significance is accentuated by the critical nature of
798 flood prediction, where precision and certainty are pivotal. Therefore, computational efficiency must be
799 viewed in the context of the broader objectives, with the accuracy and reliability of flood predictions taking
800 precedence in ensuring the safety and preparedness of the affected regions.

801 Table 9. Computational costs of N-HiTS, N-BEATS, and LSTM models in the Dog River and Killian
802 Creek gauging stations.

Model	Training Time over Train Datasets (seconds)		Predicting Time over Test Datasets (seconds)	
	Lower Dog River	Upper Dutchmans Creek	Lower Dog River	Upper Dutchmans Creek
N-HiTS	256.032	374.569	1533.029	1205.526
N-BEATS	288.511	361.599	2028.068	1482.305
LSTM	149.173	165.827	2046.140	1792.444

803
804 **4. Conclusion**
805 This study examined multiple NN algorithms for flood prediction. We selected two headwater streams with
806 minimal human impacts to understand how NN approaches can capture flood magnitude and timing for
807 these natural systems. In conclusion, our study represents a pioneering effort in exploring and advancing
808 the application of NN algorithms, specifically the N-HiTS and N-BEATS models, in the field of flood
809 prediction. In our case studies, both N-HiTS and N-BEATS models achieved state-of-the-art results,
810 outperforming LSTM as a benchmark model, particularly in one-hour prediction. While a one-hour lead
811 time may seem brief, it is highly significant for accurate flash flood prediction particularly in an area with
812 a proximity to metropolitan cities, where rapid response is critical. These benchmarking results are arguably
813 a pivotal part of this research. However, the N-BEATS model slightly emerged as a powerful and
814 interpretable tool for flood prediction in most selected events.

815 This study focused on short-lead, operational forecasting at gauged sites, using historical discharge to
816 deliver robust, low-latency updates. While the evaluation is limited to two Southeastern U.S. basins, the

817 architecture (e.g., N-HiTS) is flexible and can incorporate additional covariates and catchment attributes.
818 Extending the approach to ungauged or other basins is feasible through multi-basin training and transfer
819 learning or few-shot adaptation when even brief warm-up records are available. These extensions represent
820 promising directions for future work to assess geographic transferability under the same operational
821 assumptions.

822 In addition, the results of the experiments described above demonstrated that N-HiTS multi-rate input
823 sampling and hierarchical interpolation along with N-BEATS interpretable configuration are effective in
824 learning location-specific runoff generation behaviors. Both algorithms with an MLP-based deep neural
825 architecture with backward and forward residual links can sequentially project the data signal into
826 polynomials and harmonic basis needed to predict intense storm behaviors with varied magnitudes. The
827 innovation in this study, besides benchmarking the LSTM model for headwater streams, was to tackle
828 volatility and memory complexity challenges, by locally specializing flood sequential predictions into the
829 data signal's frequencies with interpretability, and hierarchical interpolation and pooling. Both N-HiTS and
830 N-BEATS models offered similar performance as compared with the LSTM but also offered a level of
831 interpretability about how the model learns to differentiate aspects of complex watershed-specific behaviors
832 via data. The interpretability of N-HiTS and N-BEATS arises directly from their model architecture.

833 In the interpretable N-BEATS framework, forecasts are decomposed into trend and seasonality stacks, each
834 represented by explicit basis coefficients that reveal how different temporal patterns contribute to the
835 prediction. Similarly, N-HiTS achieves interpretability by aggregating contributions across multiple distinct
836 time scales, allowing insight into the temporal dynamics driving each forecast. N-HiTS aims to enhance
837 the accuracy of long-term time-series forecasts through hierarchical interpolation and multi-scale data
838 sampling, allowing it to focus on different data patterns, which prioritizes features essential to understand
839 flood magnitudes. N-BEATS leverages interpretable configurations with trend and seasonality projections,
840 enabling it to decompose time series data into intuitive components. N-BEATS interpretable architecture
841 is recommended for scarce data settings (such as flooding event), as it regularizes its predictions through
842 projections onto harmonic and trend basis.

843 These approaches improve model transparency by allowing understanding of how each part of the model
844 contributes to the final prediction, particularly when applied to complex flood patterns. Both models also
845 support multivariate series (and covariates) by flattening the model inputs to a 1-D series and reshaping the
846 outputs to a tensor of appropriate dimensions. This approach provides flexibility to handle arbitrary
847 numbers of features. Like LSTM, both N-HiTS and N-BEATS models support producing probabilistic
848 predictions by specifying a likelihood objective. In terms of sensitivity analysis, both N-HiTS and N-
849 BEATS maintain consistent performance even when trained without specific meteorological input.

850 Although, during some flashy floods, the models encountered challenges in capturing the peak flows and
851 the dynamics of the recession curve, which is directly related to groundwater contribution to flood
852 hydrograph, both models were technically insensitive to rainfall data as an input variable. This suggests the
853 fact that both algorithms can learn patterns in discharge data without requiring meteorological input. This
854 ability underscores these models' robustness in generating accurate predictions using historical flood data
855 alone, making them valuable tools for flood prediction, especially in data-poor watersheds or even for real-
856 time flood prediction when near real-time meteorological inputs are limited or unavailable. In terms of
857 computational efficiency, both N-HiTS and N-BEATS are trained almost at the same pace; however, N-
858 HiTS predicted the test data much quicker than N-BEATS. Unlike N-HiTS and N-BEATS, LSTM excelled
859 in reducing training time due to its simplicity and limited number of parameters.

860 Moving forward, it is worth mentioning that predicting the magnitude of the recession curve of flood
861 hydrographs was particularly challenging for all models. We argue that this is because the relation between
862 base flow and time is particularly hard to calibrate due to ground-water effluent that is controlled by
863 geological and physical conditions (vegetation, wetlands, and wet meadows) in headwater streams. In
864 addition, the situations of runoff occurrence are diverse and have a high measurement variance with high
865 frequency that can make it difficult for the algorithms to fully capture discrete representation learning on
866 time series.

867 In future studies, it will be important to develop strategies to derive analogs to the interpretable
868 configuration as well as multi-rate input sampling, hierarchical interpolation, and backcast residual
869 connections that allow for the dynamic representation of flood times series data with different frequencies
870 and nonlinearity. A dynamic representation of flood time series is, at least in principle, possible by
871 generating additive predictions in different bands of the time-series signals, reducing memory footprint and
872 compute time, and improving architecture parsimony and accuracy. This would allow the model to "learn"
873 interpretability and hierarchical representations from raw data to reduce complexity as the information
874 flows through the network.

875 While a single station provides valuable localized information, particularly for small, headwater streams
876 where runoff closely follows immediate meteorological conditions, it may not capture the spatial
877 heterogeneity of larger watersheds. In our study, the applied methods successfully captured runoff
878 magnitude and dynamics in small basins for an operational setting. However, broader spatial coverage and
879 distributed data would likely enhance model accuracy for larger regions. Consequently, our conclusions are
880 specifically scoped to the selected basins and forecast horizons, and broader generalizations would require
881 multi-region investigations in future work.

882 Finally, the performance of N-HiTS, N-BEATS, or other neural network architectures could be further
883 enhanced with robust uncertainty quantification. Approaches such as Bayesian Model Averaging (BMA)
884 with fixed or flexible priors (Samadi et al., 2020) or Markov Chain Monte Carlo (MCMC) optimization
885 methods (Duane et al., 1987) could capture both aleatoric and epistemic uncertainties. We leave these
886 strategies for future exploration in the context of neural flood time-series prediction.

887

888 5. Acknowledgements

889 This research is supported by the US National Science Foundation Directorate of Engineering (Grant #
890 CMMI 2125283; [CBET 2429082](#)). All opinions, findings, and conclusions or recommendations expressed
891 in this material are those of the authors and do not necessarily reflect the views of the NSF. The authors
892 acknowledge and appreciate Thorsten Wagener (University of Potsdam, Germany) discussion and feedback
893 on this manuscript. Clemson University (USA) is acknowledged for generous allotment of computing time
894 on the Palmetto cluster.

895

896 6. Open Research

897 The historical discharge data used in this study are from the USGS
898 (https://waterdata.usgs.gov/nwis/uv/?referred_module=sw), meteorological data from USDA
899 (<https://www.ncdc.noaa.gov/cdo-web/datatools/lcd>). We have uploaded the datasets and codes
900 used in this research to Zenodo, accessible via <https://zenodo.org/records/13343364>. For
901 modeling, we used the NeuralForecast package (Olivares et al., 2022), available at:
902 <https://github.com/Nixtla/neuralforecast>.

903

904 7. References

905 Abbaspour, K.C., Yang, J., Maximov, I., Siber, R., Bogner, K., Mieleitner, J., Zobrist, J., Srinivasan, R.,
906 2007. Modelling hydrology and water quality in the pre-alpine/alpine Thur watershed using SWAT.
907 Journal of Hydrology 333, 413–430. <https://doi.org/10.1016/j.jhydrol.2006.09.014>

908 Alaa, A.M., van der Schaar, M., 2019. Attentive State-Space Modeling of Disease Progression, in:
909 Advances in Neural Information Processing Systems. Curran Associates, Inc.

910 Asquith, W.H., Roussel, M.C., Thompson, D.B., Cleveland, T.G., Fang, X., 2005. Summary of
911 dimensionless Texas hyetographs and distribution of storm depth developed for Texas Department
912 of Transportation research project 0–4194 (No. 0–4194–4). Texas Department of Transportation.

Formatted: Font: Not Bold

Formatted: Default Paragraph Font, Font: (Default)
+Headings CS (Times New Roman), 12 pt, Font color:
Auto, Pattern: Clear

913 Barnard, P.L., van Ormondt, M., Erikson, L.H., Eshleman, J., Hapke, C., Ruggiero, P., Adams, P.N.,
914 Foxgrover, A.C., 2014. Development of the Coastal Storm Modeling System (CoSMoS) for
915 predicting the impact of storms on high-energy, active-margin coasts. *Nat Hazards* 74, 1095–1125.
916 <https://doi.org/10.1007/s11069-014-1236-y>

917 Basso, S., Schirmer, M., Botter, G., 2016. A physically based analytical model of flood frequency curves.
918 *Geophysical Research Letters* 43, 9070–9076. <https://doi.org/10.1002/2016GL069915>

919 Challu, C., Olivares, K.G., Oreshkin, B.N., Garza, F., Mergenthaler-Canseco, M., Dubrawski, A., 2022.
920 N-HiTS: Neural Hierarchical Interpolation for Time Series Forecasting.
921 <https://doi.org/10.48550/arXiv.2201.12886>

922 Chen, Y., Li, J., Xu, H., 2016. Improving flood forecasting capability of physically based distributed
923 hydrological models by parameter optimization. *Hydrology and Earth System Sciences* 20, 375–
924 392. <https://doi.org/10.5194/hess-20-375-2016>

925 Clark, M.P., Nijssen, B., Lundquist, J.D., Kavetski, D., Rupp, D.E., Woods, R.A., Freer, J.E., Gutmann,
926 E.D., Wood, A.W., Brekke, L.D., Arnold, J.R., Gochis, D.J., Rasmussen, R.M., 2015. A unified
927 approach for process-based hydrologic modeling: 1. Modeling concept. *Water Resources Research*
928 51, 2498–2514. <https://doi.org/10.1002/2015WR017198>

929 CRED, n.d. EM-DAT - The international disaster database [WWW Document]. URL
930 <https://www.emdat.be/> (accessed 6.5.24).

931 Dasgupta, A., Arnal, L., Emerton, R., Harrigan, S., Matthews, G., Muhammad, A., O'Regan, K., Pérez-
932 Ciria, T., Valdez, E., van Osnabrugge, B., Werner, M., Buontempo, C., Cloke, H., Pappenberger,
933 F., Pechlivanidis, I.G., Prudhomme, C., Ramos, M.-H., Salamon, P., n.d. Connecting hydrological
934 modelling and forecasting from global to local scales: Perspectives from an international joint
935 virtual workshop. *Journal of Flood Risk Management* n/a, e12880.
936 <https://doi.org/10.1111/jfr3.12880>

937 Defontaine, T., Ricci, S., Lapeyre, C., Marchandise, A., Pape, E.L., 2023. Flood forecasting with Machine
938 Learning in a scarce data layout. *IOP Conf. Ser.: Earth Environ. Sci.* 1136, 012020.
939 <https://doi.org/10.1088/1755-1315/1136/1/012020>

940 Duane, S., Kennedy, A.D., Pendleton, B.J., Roweth, D., 1987. Hybrid Monte Carlo. *Physics Letters B*
941 195, 216–222. [https://doi.org/10.1016/0370-2693\(87\)91197-X](https://doi.org/10.1016/0370-2693(87)91197-X)

942 Erikson, L.H., Espejo, A., Barnard, P.L., Serafin, K.A., Hegermiller, C.A., O'Neill, A., Ruggiero, P.,
943 Limber, P.W., Mendez, F.J., 2018. Identification of storm events and contiguous coastal sections
944 for deterministic modeling of extreme coastal flood events in response to climate change. *Coastal
945 Engineering* 140, 316–330. <https://doi.org/10.1016/j.coastaleng.2018.08.003>

946 Evin, G., Le Lay, M., Fouchier, C., Mas, A., Colleoni, F., Penot, D., Garambois, P.-A., Laurantin, O.,
947 2023. Evaluation of hydrological models on small mountainous catchments: impact of the
948 meteorological forcings. <https://doi.org/10.5194/egusphere-2023-845>

949 Fan, C., Zhang, Y., Pan, Y., Li, X., Zhang, C., Yuan, R., Wu, D., Wang, W., Pei, J., Huang, H., 2019.
950 Multi-Horizon Time Series Forecasting with Temporal Attention Learning, in: Proceedings of the
951 25th ACM SIGKDD International Conference on Knowledge Discovery & Data Mining, KDD '19.
952 Association for Computing Machinery, New York, NY, USA, pp. 2527–2535.
953 <https://doi.org/10.1145/3292500.3330662>

954 Fang, K., Kifer, D., Lawson, K., Shen, C., 2020. Evaluating the Potential and Challenges of an
955 Uncertainty Quantification Method for Long Short-Term Memory Models for Soil Moisture
956 Predictions. *Water Resources Research* 56, e2020WR028095.
957 <https://doi.org/10.1029/2020WR028095>

958 Global assessment report on disaster risk reduction 2015 | UNDRR, 2015. URL:
959 <http://www.undrr.org/publication/global-assessment-report-disaster-risk-reduction-2015> (accessed
960 6.5.24).

961 Gotvald, A.J., 2010. Historic flooding in Georgia, 2009: U.S. Geological Survey Open-File Report 2010–
962 1230, 19 p.

963 Gupta, H.V., Kling, H., Yilmaz, K.K., Martinez, G.F., 2009. Decomposition of the mean squared error
964 and NSE performance criteria: Implications for improving hydrological modelling. *Journal of
965 Hydrology* 377, 80–91. <https://doi.org/10.1016/j.jhydrol.2009.08.003>

966 Hochreiter, S., Younger, A.S., Conwell, P.R., 2001. Learning to Learn Using Gradient Descent, in:
967 Dorffner, G., Bischof, H., Hornik, K. (Eds.), *Artificial Neural Networks — ICANN 2001*. Springer,
968 Berlin, Heidelberg, pp. 87–94. https://doi.org/10.1007/3-540-44668-0_13

969 Hsu, K., Gupta, H.V., Sorooshian, S., 1995. Artificial Neural Network Modeling of the Rainfall-Runoff
970 Process. *Water Resources Research* 31, 2517–2530. <https://doi.org/10.1029/95WR01955>

971 Jonkman, S.N., 2005. Global Perspectives on Loss of Human Life Caused by Floods. *Nat Hazards* 34,
972 151–175. <https://doi.org/10.1007/s11069-004-8891-3>

973 Kingma, D.P., Ba, J., 2017. Adam: A Method for Stochastic Optimization.
974 <https://doi.org/10.48550/arXiv.1412.6980>

975 Kratzert, F., Klotz, D., Brenner, C., Schulz, K., Herrnegger, M., 2018. Rainfall–runoff modelling using
976 Long Short-Term Memory (LSTM) networks. *Hydrology and Earth System Sciences* 22, 6005–
977 6022. <https://doi.org/10.5194/hess-22-6005-2018>

978 Lim, B., Arik, S.Ö., Loeff, N., Pfister, T., 2021. Temporal Fusion Transformers for interpretable multi-
979 horizon time series forecasting. *International Journal of Forecasting* 37, 1748–1764.
980 <https://doi.org/10.1016/j.ijforecast.2021.03.012>

981 Lobligeois, F., Andréassian, V., Perrin, C., Tabary, P., Loumagne, C., 2014. When does higher spatial
982 resolution rainfall information improve streamflow simulation? An evaluation using 3620 flood

983 events. *Hydrology and Earth System Sciences* 18, 575–594. <https://doi.org/10.5194/hess-18-575-2014>

985 MacDonald, L.H., Coe, D., 2007. Influence of Headwater Streams on Downstream Reaches in Forested
986 Areas. *Forest Science* 53, 148–168. <https://doi.org/10.1093/forestscience/53.2.148>

987 Martinaitis, S.M., Wilson, K.A., Yussouf, N., Gourley, J.J., Vergara, H., Meyer, T.C., Heinselman, P.L.,
988 Gerard, A., Berry, K.L., Vergara, A. and Monroe, J., 2023. A path toward short-term probabilistic
989 flash flood prediction. *Bulletin of the American Meteorological Society*, 104(3), pp.E585-E605.

990 McCallum, B.E., and Gotvald, A.J., 2010, Historic flooding in northern Georgia, September 16–22, 2009:
991 U.S. Geological Survey Fact Sheet 2010-3061, 4 p.

992 McCuen, R.H., Knight, Z., Cutter, A.G., 2006. Evaluation of the Nash–Sutcliffe Efficiency Index. *Journal*
993 *of Hydrologic Engineering* 11, 597–602. [https://doi.org/10.1061/\(ASCE\)1084-0699\(2006\)11:6\(597\)](https://doi.org/10.1061/(ASCE)1084-0699(2006)11:6(597))

995 Munn, M., Sheibley, R., Waite, I., Meador, M., 2020. Understanding the relationship between stream
996 metabolism and biological assemblages. *Freshwater Science* 39, 680–692.
997 <https://doi.org/10.1086/711690>

998 Nash, J.E., Sutcliffe, J.V., 1970. River flow forecasting through conceptual models part I — A discussion
999 of principles. *Journal of Hydrology* 10, 282–290. [https://doi.org/10.1016/0022-1694\(70\)90255-6](https://doi.org/10.1016/0022-1694(70)90255-6)

1000 Nevo, S., Morin, E., Gerzi Rosenthal, A., Metzger, A., Barshai, C., Weitzner, D., Voloshin, D., Kratzert,
1001 F., Elidan, G., Dror, G., Begelman, G., Nearing, G., Shalev, G., Noga, H., Shavitt, I., Yuklea, L.,
1002 Royz, M., Giladi, N., Peled Levi, N., Reich, O., Gilon, O., Maor, R., Timnat, S., Shechter, T.,
1003 Anisimov, V., Gigi, Y., Levin, Y., Moshe, Z., Ben-Haim, Z., Hassidim, A., Matias, Y., 2022. Flood
1004 forecasting with machine learning models in an operational framework. *Hydrology and Earth*
1005 *System Sciences* 26, 4013–4032. <https://doi.org/10.5194/hess-26-4013-2022>

1006 NRCS (2009). Part 630 Hydrology National Engineering Handbook, Chapter 15: Time of Concentration.

1007 Olivares, K. G., Challú, C., Garza, F., Mergenthaler Canseco, M., & Dubrawski, A. (2022).
1008 NeuralForecast: User friendly state-of-the-art neural forecasting models. PyCon Salt Lake City,
1009 Utah, US 2022. Retrieved from <https://github.com/Nixtla/neuralforecast>

1010 Olivares, K.G., Meetei, O.N., Ma, R., Reddy, R., Cao, M., Dicker, L., 2024. Probabilistic hierarchical
1011 forecasting with deep Poisson mixtures. *International Journal of Forecasting* 40, 470–489.
1012 <https://doi.org/10.1016/j.ijforecast.2023.04.007>

1013 Oreshkin, B.N., Carpov, D., Chapados, N., Bengio, Y., 2020. N-BEATS: Neural basis expansion analysis
1014 for interpretable time series forecasting. <https://doi.org/10.48550/arXiv.1905.10437>

1015 Pally, R.J., Samadi, V., 2021. Application of image processing and convolutional neural networks for
1016 flood image classification and semantic segmentation. *Environmental Modelling & Software* 148,
1017 105285. <https://doi.org/10.1016/j.envsoft.2021.105285>

1018 Palmer, T.N., 2012. Towards the probabilistic Earth-system simulator: a vision for the future of climate
1019 and weather prediction. *Quarterly Journal of the Royal Meteorological Society* 138, 841–861.
1020 <https://doi.org/10.1002/qj.1923>

1021 Park, K., Lee, E.H., 2024. Urban flood vulnerability analysis and prediction based on the land use using
1022 Deep Neural Network. *International Journal of Disaster Risk Reduction* 101, 104231.
1023 <https://doi.org/10.1016/j.ijdrr.2023.104231>

1024 Pourreza-Bilondi, M., Samadi, S.Z., Akhoond-Ali, A.-M., Ghahraman, B., 2017. Reliability of Semiarid
1025 Flash Flood Modeling Using Bayesian Framework. *Journal of Hydrologic Engineering* 22,
1026 05016039. [https://doi.org/10.1061/\(ASCE\)HE.1943-5584.0001482](https://doi.org/10.1061/(ASCE)HE.1943-5584.0001482)

1027 Refsgaard, J.C., Stisen, S., Koch, J., 2022. Hydrological process knowledge in catchment modelling –
1028 Lessons and perspectives from 60 years development. *Hydrological Processes* 36, e14463.
1029 <https://doi.org/10.1002/hyp.14463>

1030 Roelvink, D., Reniers, A., van Dongeren, A., van Thiel de Vries, J., McCall, R., Lescinski, J., 2009.
1031 Modelling storm impacts on beaches, dunes and barrier islands. *Coastal Engineering* 56, 1133–
1032 1152. <https://doi.org/10.1016/j.coastaleng.2009.08.006>

1033 Russo, S., Perraudin, N., Stalder, S., Perez-Cruz, F., Leitao, J.P., Obozinski, G., Wegner, J.D., 2023. An
1034 evaluation of deep learning models for predicting water depth evolution in urban floods.
1035 <https://doi.org/10.48550/arXiv.2302.10062>

1036 Saberian, M., Zafarmomen, N., Neupane, A., Panthi, K., Samadi, V., 2025. HydroQuantum: A New
1037 Quantum-driven Python Package for Hydrological Simulation. *Environmental Modelling &*
1038 *Software* 106736. <https://doi.org/10.1016/j.envsoft.2025.106736>

1039 Safaei-Moghadam, A., Tarboton, D., Minsker, B., 2023. Estimating the likelihood of roadway pluvial
1040 flood based on crowdsourced traffic data and depression-based DEM analysis. *Natural Hazards and*
1041 *Earth System Sciences* 23, 1–19. <https://doi.org/10.5194/nhess-23-1-2023>

1042 Saksena, S., Dey, S., Merwade, V., Singhofen, P.J., 2020. A Computationally Efficient and Physically
1043 Based Approach for Urban Flood Modeling Using a Flexible Spatiotemporal Structure. *Water*
1044 *Resources Research* 56, e2019WR025769. <https://doi.org/10.1029/2019WR025769>

1045 Samadi, S., Pourreza-Bilondi, M., Wilson, C. a. M.E., Hitchcock, D.B., 2020. Bayesian Model Averaging
1046 With Fixed and Flexible Priors: Theory, Concepts, and Calibration Experiments for Rainfall-Runoff
1047 Modeling. *Journal of Advances in Modeling Earth Systems* 12, e2019MS001924.
1048 <https://doi.org/10.1029/2019MS001924>

1049 Samadi, V., Fowler, H.J., Lamond, J., Wagener, T., Brunner, M., Gourley, J., Moradkhani, H., Popescu,
1050 I., Wasko, C., Wright, D., Wu, H., Zhang, K., Arias, P.A., Duan, Q., Nazemi, A., van Oevelen, P.J.,
1051 Prein, A.F., Roundy, J.K., Saberian, M., Umutoni, L., 2025. The Needs, Challenges, and Priorities
1052 for Advancing Global Flood Research. *WIREs Water* 12, e70026.
1053 <https://doi.org/10.1002/wat2.70026>

1054 Scott, J., n.d. Widespread Flooding After Severe Storms - WCCB Charlotte's CW. Available at:
1055 <https://www.wccbcharlotte.com/2020/02/08/widespread-flooding-after-severe-storms/> (accessed
1056 6.11.24).

1057 Sukovich, E.M., Ralph, F.M., Barthold, F.E., Reynolds, D.W., Novak, D.R., 2014. Extreme Quantitative
1058 Precipitation Forecast Performance at the Weather Prediction Center from 2001 to 2011. *Weather
1059 and Forecasting* 29, 894–911. <https://doi.org/10.1175/WAF-D-13-00061.1>

1060 Tabas, S.S., Samadi, S., 2022. Variational Bayesian dropout with a Gaussian prior for recurrent neural
1061 networks application in rainfall–runoff modeling. *Environ. Res. Lett.* 17, 065012.
1062 <https://doi.org/10.1088/1748-9326/ac7247>

1063 Thompson, C.M., Frazier, T.G., 2014. Deterministic and probabilistic flood modeling for contemporary
1064 and future coastal and inland precipitation inundation. *Applied Geography* 50, 1–14.
1065 <https://doi.org/10.1016/j.apgeog.2014.01.013>

1066 Tiwari, M.K., Chatterjee, C., 2010. Development of an accurate and reliable hourly flood forecasting
1067 model using wavelet-bootstrap-ANN (WBANN) hybrid approach. *Journal of Hydrology* 394, 458–
1068 470. <https://doi.org/10.1016/j.jhydrol.2010.10.001>

1069 Watershed Report | Office of Water | US EPA, n.d. Available at:
1070 <https://watersgeo.epa.gov/watershedreport/?comid=9224629> (accessed 6.9.24).

1071 Wee, G., Chang, L.-C., Chang, F.-J., Mat Amin, M.Z., 2023. A flood Impact-Based forecasting system by
1072 fuzzy inference techniques. *Journal of Hydrology* 625, 130117.
1073 <https://doi.org/10.1016/j.jhydrol.2023.130117>

1074 Windheuser, L., Karanjit, R., Pally, R., Samadi, S., Hubig, N.C., 2023. An End-To-End Flood Stage
1075 Prediction System Using Deep Neural Networks. *Earth and Space Science* 10, e2022EA002385.
1076 <https://doi.org/10.1029/2022EA002385>

1077 Zafarmomen, N., Alizadeh, H., Bayat, M., Ehtiat, M., Moradkhani, H., 2024. Assimilation of Sentinel-
1078 Based Leaf Area Index for Modeling Surface-Ground Water Interactions in Irrigation Districts.
1079 *Water Resources Research* 60, e2023WR036080. <https://doi.org/10.1029/2023WR036080>

1080 Zafarmomen, N., Samadi, V., 2025. Can large language models effectively reason about adverse weather
1081 conditions? *Environmental Modelling & Software* 188, 106421.
1082 <https://doi.org/10.1016/j.envsoft.2025.106421>

1083 Zhang, L., Qin, H., Mao, J., Cao, X., Fu, G., 2023. High temporal resolution urban flood prediction using
1084 attention-based LSTM models. *Journal of Hydrology* 620, 129499.
1085 <https://doi.org/10.1016/j.jhydrol.2023.129499>

1086 Zhang, Y., Pan, D., Griensven, J.V., Yang, S.X., Gharabaghi, B., 2023. Intelligent flood forecasting and
1087 warning: a survey. *ir* 3, 190–212. <https://doi.org/10.20517/ir.2023.12>

1088 Zou, Y., Wang, J., Lei, P., Li, Y., 2023. A novel multi-step ahead forecasting model for flood based on time
1089 residual LSTM. *Journal of Hydrology* 620, 129521. <https://doi.org/10.1016/j.jhydrol.2023.129521>

1090

1091